# Monolayers Studies of Mixed Films Containing Cerebrosides by Surface Tensiometry and Brewster Angle Microscopy

**THESIS**

Presented in Partial Fulfillment of the Requirements for the Degree Master of Science in the Graduate School of The Ohio State University

By

Ellen M. Adams, B.S.

Graduate Program in Chemistry

The Ohio State University

2013

Master's Examination Committee:

Prof. Dr. Heather C. Allen, Advisor

Prof. Dr. Dongping Zhong

# Abstract

In this work surface pressure-area isotherms and Brewster angle microscope (BAM) images were obtained for two-component Langmuir monolayers of bovine and porcine cerebrosides with cholesterol and palmitic acid (PA), respectively, at the air-water interface. BAM images of bovine and porcine cerebrosides reveal that condensed films form at low surface pressures. Collapse of cerebroside films resulted in line-shaped 2-D and 3-D structures. Introduction of cholesterol into bovine cerebrosides monolayers resulted in more loosely packed domains. A similar trend was observed upon the addition of PA to porcine cerebrosides. Surface morphology, collapse pressures, and collapse structures of binary films was dependent upon cholesterol or PA content. Deviations from the additivity of area and variation in collapse pressures indicate that films of cholesterol/bovine cerebrosides and PA/porcine cerebrosides are miscible.

# Dedication

*To my friends and family for their continuous support*

# Acknowledgments

I first and foremost acknowledge my advisor, Dr. Heather C. Allen, for her support and advice in pursuing this degree. I would also like to thank several members of the Allen group for their help. Dr. Dominique Verreault provided much help in proofreading parts of this thesis and providing feedback on results. Without the help and knowledge of Dana-Marie Telesford I would not know and understand BAM as well as I do. I would also like to thank Zishuai Huang for helping assemble the BAM instrument used in this thesis.

# Vita

| | |
|---|---|
| February 15, 1988 | Born – Williamsport, PA |
| May 2010 | B.S. Chemistry, Lebanon Valley College, Annville, USA |
| September 2010 – Present | Graduate Teaching Associate, Department of Chemistry and Biochemistry, The Ohio State University – Columbus, Ohio, USA |

# Publications

- E. C. Griffith, E. M. Adams, H. C. Allen, V. Vaida "Hydrophobic Collapse of a Stearic Acid Film by Adsorbed L-phenylalanine at the Air-Water Interface". *J. Phys. Chem. B*. **2012**, 116, 7849-7857

# Field of Study

Major Field: Chemistry

# Table of Contents

# List of Figures

# List of Tables

# List of Abbreviations and Symbols

## Abbreviations

| | |
|---|---|
| ADSA | axisymmetric drop shape analysis |
| BAM | Brewster angle microscopy |
| Bcerebroside | bovine cerebroside |
| C | collapse |
| CCD | charged couple device |
| CSD | constrained sessile drop |
| CWL | cutaneous water loss |
| *E. huxleyi* | *Emiliania huxleyi* |
| EM | electromagnetic |
| FAME | fatty acid methyl ester |
| FFA | free fatty acid |
| G | gaseous |
| G-LC | gas-liquid condensed |
| GDS | Gibbs dividing surface |
| GSL | glycosphingolipid |
| HFA | hydroxylated fatty acid |
| HWP | half-wave plate |
| LC | liquid-condensed |
| LE | liquid-expanded |
| LWB | Langmuir-Wilhelmy balance |
| MMA | mean molecular area |
| NFA | nonhydroxylated fatty acid |
| NA | numerical aperture |

| | |
|---|---|
| NMR | nuclear magnetic resonance |
| PA | palmitic acid |
| Pcerebrosides | porcine cerebrosides |
| PD | pendant drop |
| SC | stratum corneum |
| TAG | triacylglyceride |
| TC | titled condensed |
| UC | untilted condensed |
| WIOM | water insoluble organic matter |

## Symbols

| | |
|---|---|
| $\Gamma$ | surface excess |
| $\gamma_s$ | surface tension of surfactant monolayer |
| $\gamma_w$ | surface tension of water |
| $\lambda$ | wavelength |
| $\mu$ | chemical potential |
| $\omega$ | frequency |
| $\rho_l$ | density of subphase |
| $\rho_p$ | density of plate |
| $\theta$ | contact angle |
| $A$ | area, molecular area |
| $a$ | activity |
| $c$ | speed of light |
| $\mathbf{E}$ | electric field |
| $\mathbf{E}_0$ | amplitude (vectorial) of the electric field |
| $\mathbf{E}_i$ | electric field of the incident wave |

| | |
|---|---|
| $\mathbf{E}_r$ | electric field of the reflected wave |
| $\mathbf{E}_t$ | electric field of the transmitted wave |
| $G$ | Gibbs free energy |
| $g$ | gravity constant |
| $\mathbf{H}$ | magnetic field |
| $h$ | immersion depth |
| $\mathbf{k}$ | wave vector |
| $k_B$ | Boltzmann constant |
| $\mathbf{k}_i$ | wave vector of the incident wave |
| $\mathbf{k}_r$ | wave vector of the reflected wave |
| $\mathbf{k}_t$ | wave vector of the transmitted wave |
| $L$ | length |
| $n$ | refractive index, moles |
| $P$ | pressure |
| $r$ | position vector |
| $r_p$ | *p*-polarized Fresnel reflection coefficient |
| $r_s$ | *s*-polarized Fresnel reflection coefficient |
| $R$ | ideal gas constant |
| $R_p$ | *p*-polarized reflectance |
| $R_s$ | *s*-polarized reflectance |
| $S$ | entropy |
| $t$ | time |
| $t_p$ | *p*-polarized Fresnel transmission coefficient |
| $t_s$ | *s*-polarized Fresnel transmission coefficient |
| $T$ | temperature (absolute), thickness of plate |
| $U$ | total internal energy |
| $V$ | volume |
| $W$ | width |

# Chapter 1 Introduction

## 1.1 Overview

Cerebrosides are a type of glycosphingolipid (GSL), in which a sugar headgroup is attached to a sphingolipid, and have been isolated in several organisms including mammals, birds, plants, and echinoderms.[1–4] GSLs are typically located in the outer leaflet of cell membranes, but may also be found in the inner leaflet or within lipid vesicles, and are thought to play a role in cellular functions, specifically in cell signaling or cell recognition.[5–7] The content of GSLs in membranes varies, but is generally smaller relative to other lipids. However, large amounts (2-10% of total lipids) of GSLs are found in more specialized membranes, such as the ones found in the nervous system, and it is believed that the content of GSLs is altered in diseases of the nervous system.[8–10]

Such an alteration in cerebroside content is observed in type 2 Gaucher's disease, a condition which effects the skin. Cerebrosides are composed of a ceramide with a sugar moiety headgroup. Ceramides are produced from the cleavage of the sugar group of cerebrosides, and an inhibition of this cleavage results in drastic changes in the membrane, as has been observed in type 2 Gaucher's disease in mammals.[11] In this case, replacement of ceramides with cerebrosides leads to disruption of lipid packing in the outermost layer of the skin, the stratum corneum (SC). The abnormal lipid packing

causes in an inability to maintain moisture within the skin, and leads to a dry, scaly appearance. However, birds also have cerebrosides in their stratum corneum and do not have any abnormalities in skin structure or function.[12] The difference in skin function between the species may be due to differences in the cerebroside content and the interactions of cerebrosides with other SC lipids.

Alteration in cerebroside content due to disease is not limited to mammals. *Emiliania huxleyi (E. huxleyi)*, a type of algal bloom, dies off in large numbers when a virus causes the production of cerebrosides that do not normally exist in the organism.[13] Although cerebrosides are naturally found in biomembranes of many marine organisms, and therefore likely to be found within the biological oil slick on the ocean's surface, the production of cerebrosides in the largest algal population suggest an enrichment of cerebrosides at the ocean surface. In fact, recent studies have suggested that the majority of water insoluble organic matter (WIOM) transferred from the ocean surface to marine aerosols are complex lipids with sugar moieties.[14] It is well known that insoluble lipids generally partition to the outside of aqueous aerosols, forming an organic coating. Chemical composition and the interaction of lipids within this organic layer impact the chemical, optical, and morphological properties of the aerosol.[15,16] To date the influence of glycosylated lipids on aerosols' properties has not been well studied. Although cerebrosides have not yet been detected in marine aerosols, its interaction with other common aerosol lipids should be investigated, as it is likely that these molecules may play a role in aerosol chemistry.

In the study presented here, Langmuir films were used to investigate the 2-D phase transitions of mixed films containing cerebrosides. The morphology of these films during film compression were simultaneously visualized using Brewster angle microscopy (BAM). As cerebrosides have multifaceted relevance in biomembranes and marine aerosols, two separate systems were investigated in the interest of each one of these fields. Lipid composition in normal, healthy SC is well known, but it is not very well understood how the introduction of cerebrosides changes the interactions in SC lipids in Gaucher's disease. The SC was chosen as a biomembrane of interest, and cholesterol was used to represent a SC lipid as it one of the major components in mammalian skin. Fatty acids are very common in marine aerosols[17], and therefore palmitic acid (PA) was chosen to represent an aerosol lipid.

## 1.2 Biological Relevance

### 1.2.1 Function and Structure of the Stratum Corneum

Regulation of water content within the body is necessary to sustain life;[18] as a barrier between our body and the environment the skin is one of the most important organs in maintaining water homeostasis. Skin is composed of two layers: the dermis and epidermis (Figure 1.1). The dermis is the innermost layer of skin, and is composed of connective tissues, which anchor it to underlying subcutaneous tissues and support the epidermis. The outermost layer, the epidermis, acts as the main barrier by providing protection from environmental factors, such as ultraviolet radiation and pathogens. More

importantly, though, the epidermis controls the permeation of substances to and from the body.[19,20]

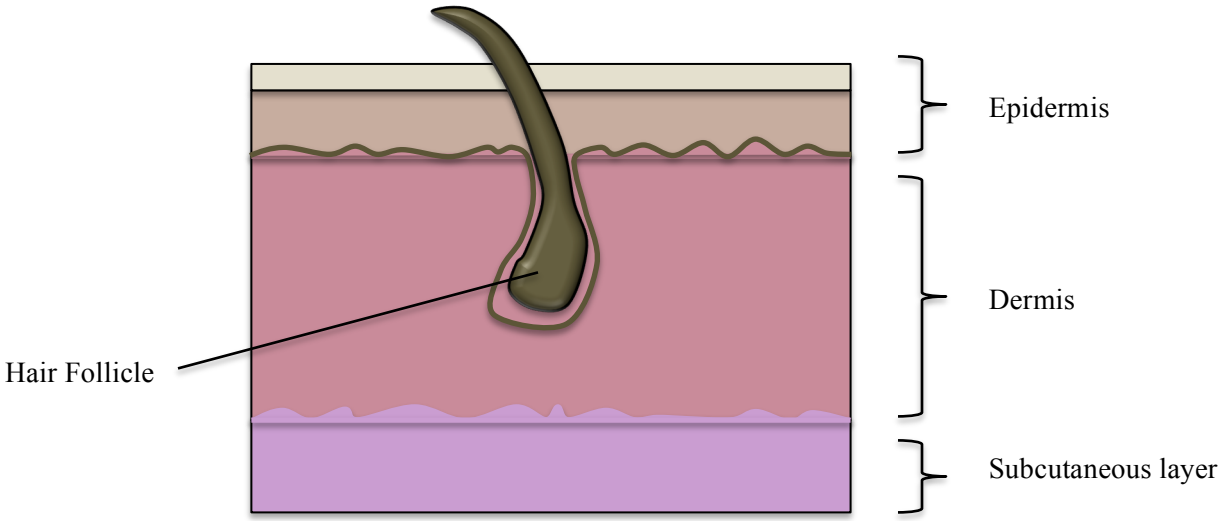


**Figure 1.1.** Diagram of skin structure.

The human epidermis is approximately 0.4-1.5 mm thick, however, this thickness can vary depending upon body location, with areas such as palms of the hand and soles of feet being thicker.[19] The epidermis is composed of several different types of cells, the majority of which are keratinocytes. As a self-renewing structure, keratinocytes are continually undergoing structural and chemical changes in a process known as differentiation. Depending upon the position and the structural properties of the keratinocyte, the epidermis can be further broken down into sublayers. The number of distinguishable layers in the epidermis varies from species to species. For instance the

human epidermis consists of four sublayers,[19,20] while birds have only two epidermal sublayers.[21] Skin thickness can also influence the number of layers, as areas with a thicker epidermis result in the presence of a fifth layer in humans.[20]

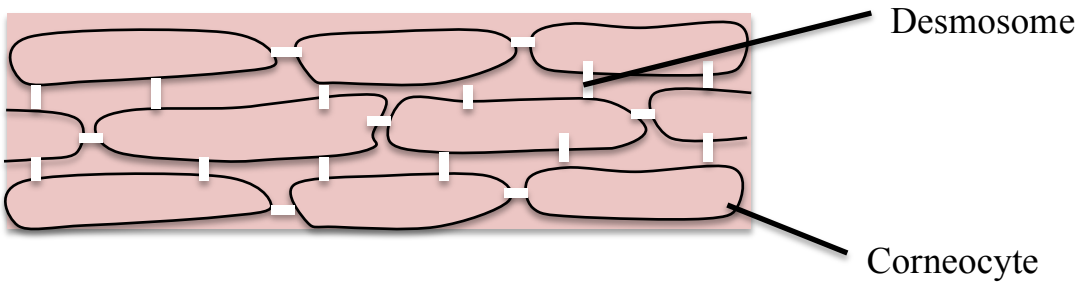


**Figure 1.2.** Diagram of epidermal layers

The epidermal layers of human skin will be further discussed here by going from the innermost to the outermost layers (Figure 1.2). The innermost, or deepest layer of the epidermis is known as the stratum basale or stratum germinativum. The stratum basale consists of a single layer of mitotically active columnar or cuboidal-shaped keratinocytes. The primary function of the stratum basale is the production of new cells. As the cells age they are pushed upwards to the next layer, the stratum spinosum. When cells enter the stratum spinsoum the differentiation process has begun. Keratinocytes become polyhedral, begin to flatten, and attach to neighboring cells through desmosomes, a proteinaceous structure. Production of keratin-containing filaments increases and intracellular lipids begin to accumulate in small organelles known as lamellar granules. As cells mature and move into the third layer of the epidermis, the stratum granulosum,

keratin-containing filaments begin to aggregate into keratohyalin granules. The final stages of keratinocyte differentiation occur in this layer. Cell organelles break down, cell content is lost, and the cell flattens out. The death of the cell results in the final epidermal layer, the SC.[19,20]

It has been shown that the SC is crucial for effective barrier function.[22] The SC not only protects from penetration of foreign substances and bacteria, but also prevents excessive water loss from underlying tissues. Winsor and Bucher were the first to show the importance of the SC when they demonstrated that disruption or removal of the SC results in increased permeability and water loss.[22] Simply put, the barrier function of the skin is localized to the SC, and therefore it controls the diffusion of water to and from the atmosphere.

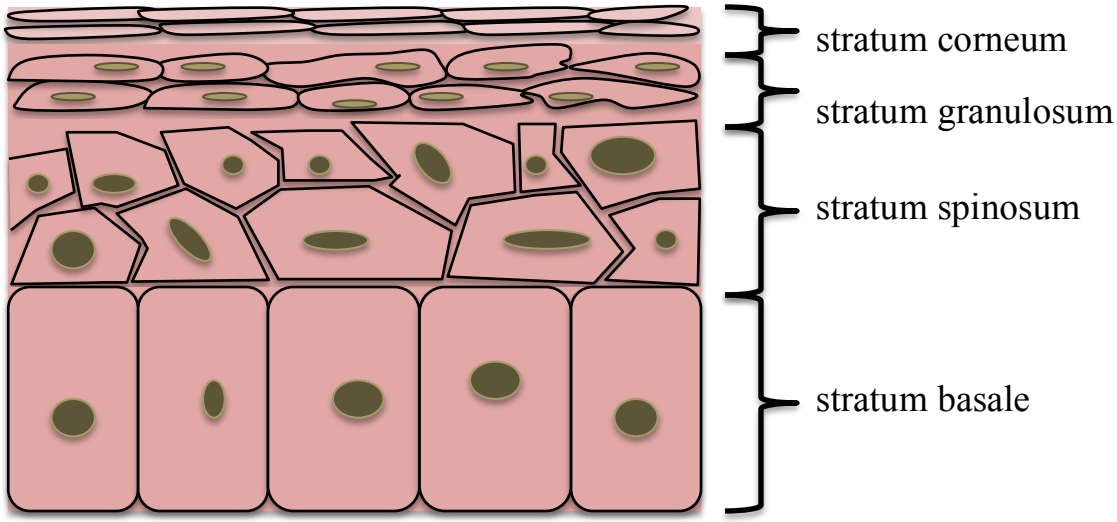


**Figure 1.3.** Brick and mortar structure of the SC

The SC is a relatively thin layer, 10-20 microns thick (depending on its water content), and is composed of corneocytes within a lipid matrix. Corneocytes are dead, flattened, protein-enriched cells derived from keratinocytes. The differentiation process results in a tightly overlapping structure usually represented by a "brick-and-mortar" model in which the corneocytes (the "bricks") are embedded in a lipid matrix (the "mortar") (Figure 1.3).[23–25] Each corneocyte is surrounded by an envelope of proteins and a bound layer of nonpolar lipids that help keep moisture inside the cell.[19,26] Neighboring corneocytes are connected by proteinaceous structures known as desmosomes that act to reinforce the "brick-and-mortar" infrastructure. These connections break down and degrade prior to exfoliation of SC cells.

Outside of the corneocytes is the lipid matrix, which is composed of hydrophobic lipid lamella. The exact organization of the lipid lamella is still largely unknown, yet several theories exist.[27–30] For instance, Forslind and Bouwstra proposed the domain mosaic and sandwich models, respectively, in which liquid crystalline and gel phases coexist. Norlen, however, argues that a single gel phase better describes the lipid organization. Although not very well understood, it has been well documented that the effective barrier function of the SC is directly linked to the intercellular lipids.[31–34] Lipid extraction studies of the SC indicate that removal of the lipids results in dry, chapped, and scaly skin that persists for up to four days. A significant decrease in water content is correlated with the appearance of dry skin.[34] Such studies suggest that the ability of the skin to maintain water homeostasis is related to the content and organization of the SC intercellular lipids.

### 1.2.2 Intercellular Lipids in the Stratum Corneum

*Lipids in Human Stratum Corneum*

Despite their importance in the SC, intercellular lipids only make up approximately 10% of the total dry mass.[35] The majority of these lipids are synthesized *in situ*. During the differentiation process lipids within keratinocytes gather in lamellar granules. At this stage the lipids are a complex mixture comprised of phospholipids, glycosylceramides, ceramides, free fatty acids, and cholesterol.[36] Towards the end of

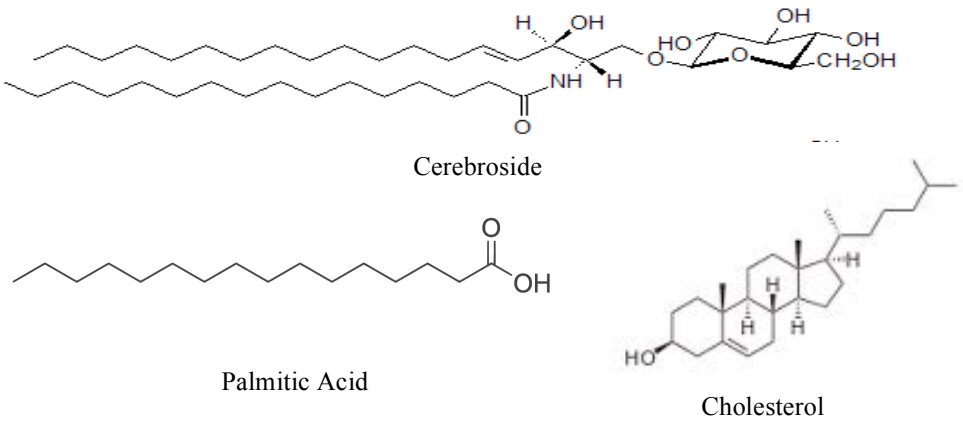


**Figure 1. 4.** Structures of lipids found in the SC of type 2 Gaucher's disease.

differentiation the lamellar granules migrate to the cell wall, where they break open and their contents extrude into the intercellular spaces. Also contained within the lamellar granules are hydrolytic enzymes, such as acid phosphatase and β-glucocerebrosidase, which begin to degrade larger lipids upon extrusion.[37,38] The SC is therefore void of any phospholipids or glycosylceramides.[36] After differentiation the SC has three main lipid

components: free fatty acids (FFAs) (10-15%), cholesterol (25-30%), and ceramides (50%). Cholesterol sulfate and cholesterol esters are also present, but typically make up less than 5% each.[36,39,40] Composition of these lipids varies regionally over the body. For instance, areas with high water permeability, such as the sole of the foot, typically have a higher content of ceramides compared to areas with less water permeability, such as the face.[41]

A variety of (FFAs) have been found in the SC. The majority of them are straight-chained and saturated, although a few monounsaturated species have been identified. Long-chained species of eighteen carbons or more are typical, with twenty-four carbons being the most abundant (Table 1.1).[42,43] Fatty acids are the only ionizable lipids within the SC other than cholesterol sulfate. This may be attributed to the acidic pH of the SC, which varies from 4-6. Others believe the ionizable headgroup may help facilitate lipid lamella formation.[28,44]

**Table 1.1.** FFA composition in the SC.[42]

| Chain Structure | Percent (wt%) |
|---|---|
| 14:0 | 0.8 |
| 15:0 | 0.7 |
| 16:0 | 7.4 |
| 16:1 | 0.7 |
| 17:0 | 0.8 |
| 18:0 | 9.1 |
| 18:1 | 5.7 |
| 18:2 | 1.4 |
| 19:0 | 1.1 |
| 20:0 | 5.9 |
| 21:0 | 1.9 |
| 22:0 | 15.3 |
| 23:0 | 6.2 |
| 24:0 | 26.9 |
| 25:0 | 5 |
| 26:0 | 8.5 |
| 28:0 | 2.7 |

Cholesterol has long been recognized as a ubiquitous molecule in membranes. Depending upon its abundance and the composition of the other components, cholesterol can cause membranes to become more or less rigid.[44,45] The ability of cholesterol to make a membrane more rigid, or more ordered, is known as condensation. An ordered membrane has lipids that are tightly packed together with little defects, which makes the membrane less permeable. While the exact molecular organization of lipids in the SC is not known, cholesterol may promote efficient packing of lipid lamella to decrease pores and channels through which water can travel.

Ceramides are a type of sphingolipid, a molecule consisting of a free fatty acid amide-linked to a sphingosine base. Nine different types of ceramides have been isolated in human SC with structural variances occurring in the polar headgroup and acyl chain

length.[40] Typically the fatty acid chain is twenty carbons or longer and saturated, however, the chain length can range from fourteen to thirty carbons.[46,47] Due to the lengthy acyl chains ceramides are practically insoluble. The highly hydrophobic nature of these molecules makes them ideal components in barriers, and they are typically found in cell membranes. However, ceramides usually make up a small fraction of cell membranes.[48] The high abundance of ceramides in the SC is unique, and may explain its ability to effectively slow water diffusion.

*Lipids in Avian Stratum Corneum*

Compared to mammals, the intercellular lipids of birds constitute a larger variety of lipids (Table 1.2).[12,39] Primarily these lipids include ceramides, cerebrosides, cholesterol esters, cholesterol, FFAs, fatty acid methyl esters (FAMEs), and triacylglycerides (TAGs).[12,21,49,50] The composition of lipids in avian SC varies widely between species of birds, as can be seen in Table 1.3. For example, in the hoopoe lark, a desert bird, cerebrosides make up 31% of lipids, while in the skylark, a mesic bird, cerebrosides constitute only 12%.[12] Similar to humans, sphingolipids are typically the most abundant lipids, representing 40% of lipids. However, birds contain two distinct sphingolipids: ceramides and cerebrosides, a ceramide with a sugar moiety headgroup. The percentage of ceramides in birds is substantially less than for humans, and is reported to be approximately 15% while cerebrosides account for the other 25%.[21] Like ceramides, cerebrosides can have structural variances in headgroup and chain length size. A wide

array of both ceramides and cerebrosides are found in birds. In house sparrows alone 79 molecular species of ceramides and 97 cerebrosides have been identified.[4]

**Table 1.2.** Percent composition of lipids in SC in various species.[12,39]

| Lipid | Human | Pig | Bird |
|---|---|---|---|
| Ceramide | 50 | 49.2 | 15 |
| Cholesterol | 25-30 | 19.6 | ≤ 5 |
| FFA | 10-15 | 26 | 1-30 |
| Cholesterol Ester | ≤ 5 | 0.7 | 4-20 |
| Cholesterol Sulfate | ≤ 5 | | ≤ 1 |
| TAG | | 2.6 | 1-30 |
| Cerebroside | | | 25 |
| FAME | | | 1-30 |
| Unidentified | | 1.9 | |

**Table 1.3.** Percent composition of lipids in SC in various birds.[12]

| Lipid | Hoopoe Lark | Desert Lark | Skylark | Scarlet Tanager |
|---|---|---|---|---|
| Cholesterol Ester | 11.7 | 9.2 | 6.0 | 4.7 |
| FAME | 5.1 | 7.7 | 4.7 | 30.3 |
| TAG | 13.5 | 12.7 | 31.1 | 14.3 |
| FFA | 14.6 | 17.6 | 30.3 | 1.3 |
| Cholesterol | 3.8 | 5.1 | 4.1 | 0.8 |
| Ceramides | 19.9 | 18.5 | 11.2 | 28.3 |
| Cerebrosides | 31.4 | 29.2 | 12.6 | 16.2 |
| Cholesterol Sulfate | 0 | 0 | 0 | 4.1 |

A notable difference between birds and humans is that cholesterol constitutes a much smaller percentage of lipids, typically less than 5%. Cholesterol esters are much more abundant, ranging between 4-20%. FFAs, FAMEs, and TAGs all exhibit a wide range in composition, between 1-30%, depending upon the bird species.[12,50] Variations in composition and abundance of intercellular lipids in birds and humans suggests that the organization of lipid lamellae in these two species may be very different, which may lead to differences in permeability and water content.

### 1.2.3 Gaucher's Disease

Gaucher's disease is a rare, genetically inherited condition in mammals caused by a deficiency in the enzyme β-glucocerebrosidase. This enzyme is responsible for the cleavage of sugar moieties on cerebrosides to convert them to ceramides. The absence, inhibition or mutation of β-glucocerebrosidase results in an accumulation of cerebrosides, which is why Gaucher's disease is typically referred to as a lipid storage disease.[51–53] Accumulation of cerebrosides most commonly occurs in the spleen, liver, lungs, bone marrow, skin, and central nervous system.[51,54] Depending upon the symptoms presented, Gaucher's disease may be divided into three types. Type 1 has a notable absence of neurological symptoms.[55] Both Type 2 and Type 3 present neurological symptoms, but are distinguished by the severity of the symptoms and age of symptom onset.[51]

Type 2 is the most severe form of Gaucher's disease in which death typically occurs within the first two years of life. Neurological abnormalities usually do not develop for a few months, but the majority of infants with type 2 Gaucher's disease are

born with congenital ichthyosis, a non-contagious skin disease in which the skin is extremely dry, scaly, peeling, or shiny in appearance.[56–59] Animal models of type 2 Gaucher's disease in rats and mice also confirm the presence of abnormal skin at birth.[60] Investigation of skin samples from both humans and mice reveal irregular, loosely packed lipid lamellae within the SC.[61] Disruption of lipid lamellae formation leads to decreased barrier function, including increased water loss[62], and may explain the observation of dry, scaly skin in Gaucher's type 2 newborns.

The inability to form an efficient permeability barrier in type 2 Gaucher's disease has been attributed to the replacement of ceramides with cerebrosides, in which the bulky sugar headgroup of cerebroside may disrupt lipid packing and hydrogen-bonding networks.[12] Notable, however, is that the presence of cerebrosides in avian SC does not result in disordered lipid packing or decreased hydration. In fact, cutaneous water loss (CWL) in birds has been correlated with cerebroside content.[12] Mesic sparrows from Ohio were observed to have higher rates of CWL compared to sparrows from a desert environment.[12,49] Thin-layer chromatography of SC samples from these same birds revealed that mesic sparrows contain a significantly smaller percentage of cerebrosides compared to desert sparrows. Therefore the difference in CWL among bird species may be due to the cerebroside content, in which birds with higher cerebroside content lose less water through the skin.[12] Contrary to mammals, the presence of cerebrosides in avian SC promotes skin hydration. The lack of hydration in mammals with type 2 Gaucher's disease may not simply be due to the presence of cerebrosides, but rather to the interaction of cerebrosides with other intercellular lipids. Differences in cerebroside

content between humans and birds may account for the observed dissimilarities in skin functionality, as a certain amount of cerebroside may facilitate better packing and hydrogen bonding with other lipids. In order to better understand why type 2 Gaucher's disease results in abnormal skin function, it is imperative to understand the complex interactions of cerebrosides with other SC lipids.

## 1.3 Atmospheric Relevance

It is well known that marine aerosols contain a complex mixture of organic materials. Marine aerosols are formed during bubble bursting at the ocean surface. The ocean surface is a biological oil slick, resulting from the rise of hydrophobic cellular components upon marine organisms death and decomposition. Typically organic compounds in the oil microlayer are attributed to the breakdown of biological membranes, which are mostly comprised of phospholipids. Several organic compounds, including FFAs, fatty alcohols, sterols, amino acids, polycyclic aromatic hydrocarbons, and carbohydrates have been identified.[63–66] However, the ocean surface is not limited to simple organic compounds, as more complex molecules such as proteins, bacteria, and viruses are also present.[67–69]

Evidence has shown that aqueous aerosols, both from marine and continental sources, have an organic layer coating the aerosol.[17,70] Such aerosols are proposed to have an inverted micelle structure, in which the aqueous core is encased by a layer of hydrophobic lipids.[66,71,72] The polar headgroup of the insoluble lipids face the aqueous core while the hydrophobic portion faces the atmosphere. Nuclear magnetic resonance

(NMR) measurements of primary marine aerosols indicate that the WIOM is primarily composed of lipopolysaccharides or other sugar-like compounds.[14] The presence of lipopolysaccharides is mostly attributed to exudates of phytoplankton, which inhabits the upper layer of the ocean.[73]

Lipopolysaccharides are large, complex molecules consisting of lipids covalently linked to polysaccharides. As a major component in marine aerosols, it is important to understand the interactions of lipopolysaccharides with other aerosol lipids. The phase and structure of aerosols influence reactions of organic compounds, such as oxidation, which then affect their chemical, optical, and morphological properties.[74] Composition of the organic film also influences surface morphology, as soluble surfactants form expanded films and insoluble surfactants form close-packed films.[15,66] Packing of the surface film affects uptake and evaporation of the water, which can then alter other properties of the aerosol.[16,75] It is imperative to understand the interactions of lipopolysaccharides with other lipids and how those interaction effect aerosol properties. However, due to the large size and complex composition of lipopolysaccharides, the use of a simpler organic molecule may be more practical.

Cerebrosides are the simplest water insoluble surfactants containing saccharide groups, composed of two alkyl chains and a polar sugar headgroup. The structure of cerebroside molecules is better characterized than lipopolysaccharides, which may make interpretation of its interactions easier. Similar to lipopolysaccharides, cerebrosides are often found in marine environments. Cerebrosides are a typical component of membranes in marine organisms[76], and are especially important in algal blooms. *E. huxleyi* is a type

of coccolithophore, which form abundant algal blooms.[77] These algal blooms have a significant impact on atmospheric chemistry, as they are a large carbon sink and a major source of dimethysulfide.[78] In recent years, large numbers of these algal blooms have been mysteriously dying off. It was determined that the virus EhV-86 in conjunction with its host, *E. huxleyi*, produce a cerebroside whose introduction cause cell apoptosis.[13,78] Due to the production of cerebrosides in these algal blooms, it is likely that they would be found in the microlayer of the ocean's surface. Therefore cerebrosides are also most likely to be incorporated into marine aerosols. Investigation of cerebrosides at an aerosol surface and their interactions with other lipids is important in understanding how glycosylated lipids may affect aerosol properties.

## 1.4 Objectives

In this study, Langmuir monolayers were used as a laboratory model for SC lipids and aerosol surfaces at an air-water interface. The main focus of this study is the interaction of cerebrosides with other lipids. Results presented in Chapter 4 probe the interaction, organization, and surface morphology of these lipid mixtures. The techniques used in these studies, surface tensiometry and Brewster angle microscopy (BAM), are discussed in detail in Chapters 2 and 3.

# Chapter 2 Theory and Instrumentation

## 2.1 Surface Tensiometry

### 2.1.1 Gibbs Adsorption Equation

A Langmuir monolayer can be thought of as a transition region between two bulk phases. It can be expected that this transition region is very inhomogeneous and that the thermodynamic properties of this region vary from those of the bulk phases. The Langmuir monolayer, or real system, can be represented by a liquid column in which two bulk phases α and β, are separated by an interfacial region, s. Each bulk phase contains a

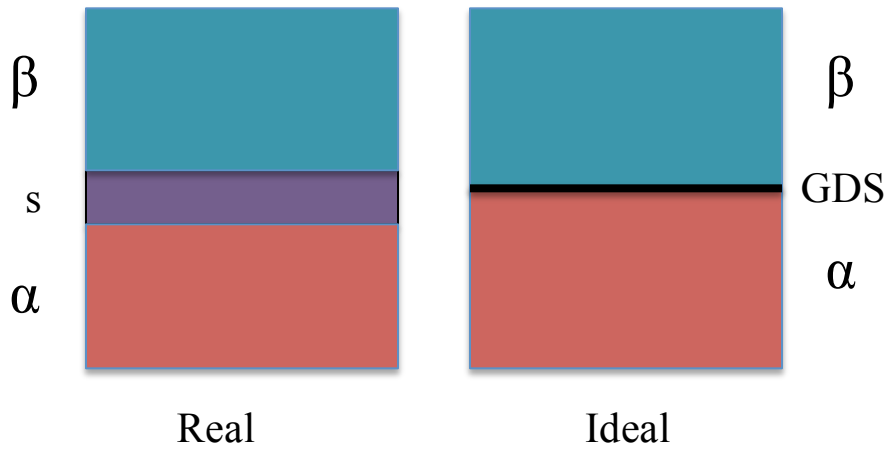


**Figure 2.1.** Liquid columns of real and ideal systems

number of components, $n_i$. This real liquid column can be compared to an ideal liquid column, in which the two bulk phases are not separated by an interface, but by an arbitrary, mathematical plane known as the Gibbs dividing surface (GDS). The bulk properties of the α and β phases remain unchanged up until the dividing surface. For the real system the total number of moles remains fixed. However, for the ideal system the number of moles in α and β vary depending upon the placement of the GDS. This means that in the real system there may be excess of moles that is more, less, or equal to the reference system. This excess is termed the surface excess and applies to all extensive properties of the interface.

The total Gibbs free energy of a real system with an interface can be written as the sum of the Gibbs energy of the bulk and surface regions (Eq. 2.1).

$$G^T = G^\alpha + G^\beta + G^S \tag{2.1}$$

where $G^\alpha$, $G^\beta$, and $G^S$ can be each be expressed based on the thermodynamic definitions

$$G^\alpha = U^\alpha + P^\alpha V^\alpha - TS^\alpha + \sum_{i=1}^{N} n_i^\alpha \mu_i^\alpha \tag{2.2}$$

$$G^\beta = U^\beta + P^\beta V^\beta - TS^\beta + \sum_{i=1}^{N} n_i^\beta \mu_i^\beta \tag{2.3}$$

$$G^S = U^S + P^S V^S - TS^S + \sum_{i=1}^{N} n_i^S \mu_i^S + A\gamma \tag{2.4}$$

Where $U$ is the internal energy, $P$ is the pressure, $V$ is the volume, $T$ is the temperature, $S$ in the entropy, $\mu$ is the chemical potential, $A$ is the area of the dividing surface, and $\gamma$ is the surface tension. Substitution of Eqs. (2.2)-(2.4) into Eq. (2.1), followed by differentiation leads to

$$dG^T = Ad\gamma + \gamma dAi + \sum_{\alpha,\beta,S}\left(dU + VdP + PdV - SdT - TdS + \sum_{i=1}^{N} n_i d\mu_i + \sum_{i=1}^{N} \mu_i d\, n_i\right) \tag{2.5}$$

From the first law of thermodynamics the internal energy of bulk phases can be expressed as

$$\begin{aligned} dU^{\alpha,\beta} &= \delta q^{\alpha,\beta} + \delta w^{\alpha,\beta} \\ &= TdS^{\alpha,\beta} - P^{\alpha,\beta} dV^{\alpha,\beta} \end{aligned} \tag{2.6}$$

where $\delta q$ and $\delta w$ are heat and work. It is assumed that the process is reversible. For the surface region an additional term is added to account for non-PV work.

$$\begin{aligned} dU^S &= \delta q + \delta w \\ &= TdS - PdV - \gamma dA \end{aligned} \tag{2.7}$$

Substitution of Eqs. (2.6)-(2.7) into Eq. (2.5) results in simplification of the expression for $dG^T$, which can now be written as

$$dG^T = Ad\gamma + \left( \sum_{\alpha,\beta,S} VdP - SdT + \sum_{i=1}^{N} n_i \, d\mu_i + \sum_{i=1}^{N} \mu_i dn_i \right) \tag{2.8}$$

According to the Gibbs-Duhem equation, the total Gibbs energy differential can be expressed as[79]

$$dG^T = VdP - SdT + \sum_{i=1}^{N} \mu_i dn_i \tag{2.9}$$

Substitution of Eq. (2.9) into Eq. (2.8) results in the following expression

$$0 = Ad\gamma + \sum_{\alpha,\beta,S} n_i \, d\mu_i \tag{2.10}$$

The Gibbs-Duhem equation assumes that equilibrium has been reached. For bulk phases the change is chemical potential is constant, and therefore the second term in Eq. (2.10) goes to zero for α and β. The equation then reduces to

$$0 = Ad\gamma + \sum_{i=1}^{N} n_i^s d\mu_i \tag{2.11}$$

or

$$0 = d\gamma + \sum_{i=1}^{N} \Gamma_i^s d\mu_i \tag{2.12}$$

where $\Gamma_i^s$ is the surface excess and can be defined as

$$\Gamma_i^s \equiv \frac{n_i^S}{A} \tag{2.13}$$

The value of $\Gamma_i^s$ is dependent upon the position of the arbitrary GDS. In order to make $\Gamma_i^s$ have a more physical meaning the GDS can be shifted. For example, in a binary system with components $n_1$ and $n_2$, the GDS surface can be fixed such that the value of $\Gamma_1 = 0$. Simplification and rearrangement of Eq. 2.12 now gives to

$$-d\gamma = \Gamma_2^s d\mu_2 \tag{2.14}$$

where $\Gamma_2$ is the relative surface excess of component 2. The surface excess value can still be positive, negative, or zero.

The chemical potential is related to the activity and can be expressed as

$$\mu_2 = \mu_2^\circ + RT ln\, a_2 \tag{2.15}$$

where $\mu_2^\circ$ is the chemical potential of the pure state, $R$ is the gas constant, and $a$ is activity. Differentiation of the chemical potential gives the equation

$$\begin{aligned} d\mu_2 &= RT d(ln\, a_2) \\ &= \frac{RT}{a_2} da_2 \end{aligned} \tag{2.16}$$

Substitution of Eq. (2.16) into Eq. (2.14) followed by rearrangement results in

$$\Gamma_2^S = -\frac{a_2}{RT}\frac{d\gamma}{da_2} \tag{2.17}$$

Eq. (2.17) is the Gibbs adsorption equation. It relates the surface excess of component 2 to the activity of component 2.

### 2.1.2 Surface Free Energy and Surface Tension

As mentioned earlier the interfacial region is a very inhomogeneous region and is expected to have very different thermodynamic properties than bulk phases. As seen earlier the differential Gibbs free energy of the surface can be expressed as

$$dG^S = VdP - SdT + \sum_{i=1}^{N} n_i d\mu_i + \gamma dA \tag{2.18}$$

The same differential can be expressed as a sum of partial differentials

$$dG^S = \left(\frac{\partial G^S}{\partial P}\right)_{T,A,n_i} dP + \left(\frac{\partial G^S}{\partial T}\right)_{P,A,n_i} dT + \left(\frac{\partial G^S}{\partial A}\right)_{T,P,n_i} dA \tag{2.19}$$

From comparison of the two $dG^S$ expressions it can be seen that surface tension is the work it takes to change the area of the surface under reversible and isothermal conditions.

$$\gamma = \left(\frac{\partial G^S}{\partial A}\right)_{T,P,n_i} \tag{2.20}$$

Physically surface tension is the reduction of the interfacial area in order to minimize the high energy of the surface. In bulk phases, molecules have many neighboring molecules, which equally pull the molecule in all directions. This results in a net force of zero for that molecule. However, if that molecule is found at an interface, it does not have the same amount of neighboring molecules. Therefore forces on the molecule do not cancel out, resulting in a non-zero net force. To accommodate for this higher energy the molecule is pulled towards the bulk, and reduces the interfacial area.[79,80]

### 2.1.3 Methods of Measuring Surface Tension

Several different methods can be used to measure surface tension. While all methods have advantages and disadvantages, the practicality of the method used depends on the system being studied. For example, the constrained sessile drop (CSD) is more suited for studying lung surfactants because it can better replicate the repetition fast compression/expansion cycles of the lung alveoli. However, this same method would not be ideal for determining the correlation between surface tension and surface morphology. Some of these methods will be discussed below. Langmuir-Wilhelmy balance (LWB) method will be focused on as this technique is used in the studies presented here.

The most common method for measuring surface tension is LWB. Typically this method has an instrumental setup that incorporates a Langmuir trough, movable barriers and a Wilhelmy plate tensiometer. A Langmuir film is created by dissolving the sample in an organic solvent, and then depositing the sample on the trough subphase.

Evaporation of the organic solvent leaves behind a one molecule thick layer or monolayer of the sample on the surface. Movement of the barriers results in changes in the physical state of the monolayer, which is detected by changes in the surface pressure. The surface pressure is a difference in surface tensions and is given by[80]

$$\pi = \gamma_W - \gamma_S \tag{2.21}$$

where $\gamma_W$ is the surface tension of the subphase, and $\gamma_S$ is the surface tension of the subphase covered with a monolayer.

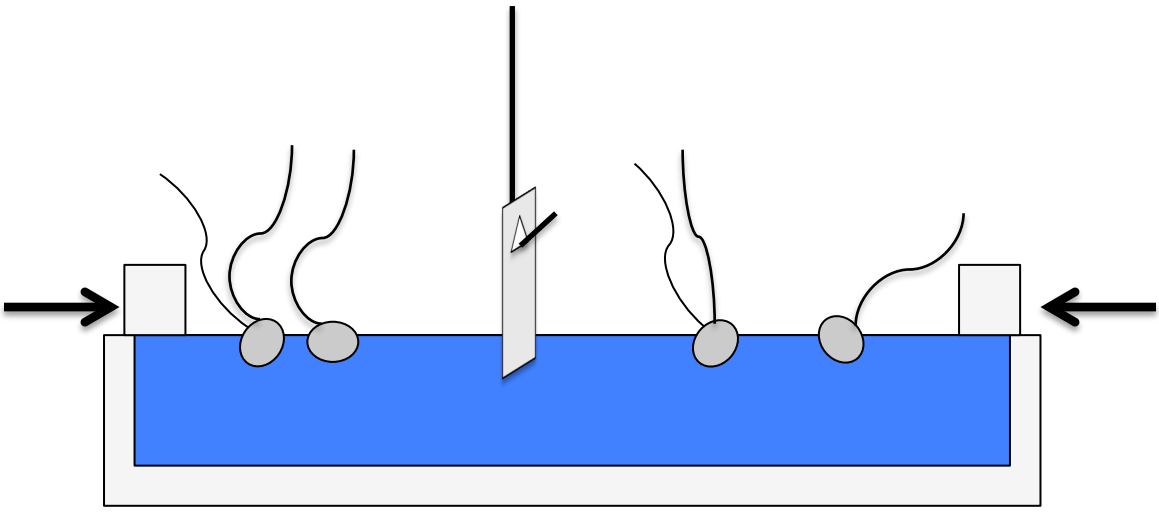

**Figure 2.2.** Schematic diagram of Langmuir-Wilhelmy balance setup

Surface tension, with or without the surfactant monolayer, is measured by the Wilhelmy plate. Traditionally the Wilhelmy plate is made of platinum due to its sensitivity and ability to be easily cleaned. However, filter paper plates are also a very common material. The Wilhelmy plate is suspended such that the plate is partially

immersed in the liquid surface. Forces act on the plate and include gravity, buoyancy, and surface tension. The net downward force is dependent upon the width (*W*), length (*L*), and thickness (*T*) of the plate, and can be given as[80]

$$F_{net} = F_{gravitational} + F_{surface} + F_{bouyancy} = \rho_p LWT + 2\gamma_W(T + W)cos\theta - \rho_l gTWh \quad (2.22)$$

where $\rho_p$ is the density of the plate, $g$ is the gravitational constant, θ is the contact angle of the liquid on that plate, $\rho_l$ is the density of the subphase, and $h$ is the immersion depth Assuming that the contact angle is such that the plate in completely wetted (θ =1) the net downward force of the subphase and the subphase with monolayer can be measured. Differences in the net downward forces give rise to Eq. (2.21).

The LWB method has several advantages. Experimental conditions such as temperature, compression rate, pH, and subphase composition can be altered in a controlled manner. The Langmuir trough can be easily integrated into spectroscopic setups, allowing more information to be collected simultaneously. However, there are disadvantages to using this technique. The amount of sample deposited on the surface must be relatively small, typically in the microliter range. Leakage of the sample or subphase is common, and results from a meniscus inversion.[81]

Drop shape techniques are a very common way to measure surface tension and a few will be discussed here. The pendant drop (PD) method is one of the oldest drop method techniques, and is said to have the greatest accuracy in determining surface tension.[82] In this method a liquid drop is suspended from a capillary tube or needle. A

charge coupled device (CCD) camera is typically used to record images of the drop throughout the experiment. The surface tension is determined from the shape of the drop, which can be described with the Laplace-Young equation (Eq. 2.23) [83,84]

$$\Delta P = \gamma \left( \frac{1}{R_1} + \frac{1}{R_2} \right) \tag{2.23}$$

where $\Delta P$ is the pressure differential across the droplet surface, and $R_1$ and $R_2$ are the inner and outer radii of the droplet. Drop shape is dependent upon the balance of gravitational and surface forces. For example, if the net forces on the drop are due to gravity, the drop tends to be elongated. However if surface forces have a greater effect, then the drop becomes round in shape.[85] With the use of axisymmetric drop shape analysis (ASDA) a value for surface tension can be determined by numerically fitting the shape of the droplet to a profile generated by the Laplace equation.[86]

The PD drop method has the main advantage that it is a simple experimental setup. It is also not limited by the concentration of the surfactants. Therefore real life physiological and environmental concentrations can be studied. Drops are typically well formed due to gravity, however drops tend to detach from the capillary tube if they become too large. Film leakage is also an issue at low surface tensions.[87,88]

Another drop shape method is CSD. In this method a sessile droplet is formed on top of a small, circular pedestal. The pedestal has knife-sharp edges to prevent leakage of the droplet. The droplet can be expanded and contracted as necessary by a computer-controlled stepper motor that operates the delivery syringe. This allows rapid cycling of

the droplet size. Typically, the CSD setup is enclosed in a chamber to prevent contamination and control temperature and humidity. Images of the sessile drop are recorded continuously throughout the experiment with a CCD camera. Similar to the PD method, fitting of the sessile drop shape with a Laplace theoretical profile is used to determine surface tension.[86,89] CSD has the advantage over other drop methods in that film leakage is not an issue. Incorporation of a second syringe allows replacement of bulk materials, which makes this method more applicable to real world systems, such as aerosols. The use of ADSA gives an accurate measurement of surface tension.[87,88] However, ADSA begins to breakdown if droplets are too spherical. This is a limitation observed in all droplet techniques.[85]

### 2.1.4 2-D Phases in Langmuir Monolayers

Langmuir monolayer studies can provide information other than surface tension, as it has been shown that monolayers behave as a quasi-2-D phases analogous to 3-D liquid, solids, and gases. Similar to 3-D analogs, changes in temperature or pressure can change a 2-D liquid to another phase. However, in this case, surface pressure is the 2-D analog of pressure. Surface pressure is the result of molecular interactions in the monolayer and between the monolayer and subphase. Reduction of the mean molecular area per molecule changes the surface pressure as molecules have increased interactions and changes in orientation. A surface pressure-molecular area ($\pi$-A) isotherm can be produced, which gives information about the monolayer, including phase changes and stability. The shape of the isotherm is dependent upon the nature of the surfactant in question. Molecular interactions of alkyl chains (van der Waals forces), polar headgroups

(electrostatic forces), and the interaction of the subphase with headgroups (e.g. hydrogen-bonding) influence the phases.[80] Some 2-D phases observed for molecules in this study will be discussed below.

*Gaseous Phase*

Langmuir monolayers are typically spread such that the molecules exist in a gaseous (G) phase. Molecules are far apart, resulting in negligible van der Waals forces due to alkyl chain interactions. Polar headgroup regions also have little interaction leading to reduced electrostatics. It is thought that molecules are arranged in such a way that the alkyl chains are nearly flat to the subphase surface. Despite being in the gas phase, most substances have sufficient interactions with the subphase to be nonvolatile. Molecules in the monolayer move with an average translational kinetic energy of $\frac{1}{2}k_BT$, where $k_B$ is the Boltzmann constant, for each degree to freedom. The surface pressure is assumed to be produced by movement of molecules in the two dimensions of the surface plane, leading to a 2-D version of an ideal gas equation,

$$\pi A = k_B T \qquad (2.24)$$

where $A$ is the mean molecular area.[79,80]

*Liquid Phases*

As monolayers are compressed to smaller molecular areas, two distinguishable liquid phases may be observed, the liquid-expanded (LE) and liquid-condensed (LC)

phases. Compression of the trough barriers brings the molecules closer together, resulting in increased interactions between alkyl chains, which are randomly oriented. Interactions between polar headgroups are still negligible. Molecules with such an arrangements are in the LE phase. Typically the G to LE phase transition is marked by an increase in surface pressure with considerable curvature in the π-A isotherm.[79,80]

Further compression of the trough barriers results in the transition from a LE to a LC film. Molecules in the LC phase have considerable interactions between alkyl chains, where alkyl chains are nearly upright, well ordered, and closely packed. Compressibility is greatly reduced in the LC phase, as the slopes of the π-A plots are nearly straight or steep in this region of the isotherm.[79,80] More than one LC phase may occur during compression, as has been observed for fatty acid monolayers. In this case two LC phases are seen, where first alkyl chains are closely packed but tilted with respect to the surface plane. Further compression forces the alkyl chains completely perpendicular to the surface, and is observed by a kink in the π-A isotherm.

*Collapse Phase*

As monolayers films are compressed a limiting value is reached at which the film can no longer be compressed and a sudden decrease in surface pressure is observed. At this point the monolayer begins to form 3-D structures and has entered a new phase, called the collapse (C) phase. The mechanism by which collapse occurs depends upon the nature of the film, temperature, and the compression rate.[90–93] Collapse of the monolayer is usually an irreversible process. However, some films have reversible collapses, in

which the collapse structure is reincorporated into the monolayer upon film expansion.[94] The collapse mechanism determines whether the phase transition is reversible or irreversible.

Generally irreversible collapse occurs through one of two processes, solubilization or fractionization. Fractionization typically occurs for rigid films, occurs at higher surface pressures, and results in the formation of 3-D aggregates at the air side of the film. Solubilization is the ejection of monolayer material into the subphase and typically occurs at lower surface pressures. Fluid films are subject to this type of collapse.[94,95] For both of these processes reincorporation of material back into the monolayer is not possible. Imaging techniques along with X-ray diffraction studies have shown a variety of structures resulting from these mechanisms, including lipid aggregates, vesicles, tubes, bilayers, and trilayers.[91,96–99]

Reversible collapse is known to occur through only one mechanism: folding. In this case compression to high surface densities leads to buckling of the monolayer. Buckles coexist with flat portions of the monolayer until further compression causes the edges of the buckles to fuse to form a bilayer fold.[94,95,100,101] Formation of these folds may project in either direction, i.e. into the subphase or air. The folding mechanism was first thought to only occur at the phase boundary between coexisting LE and LC islands.[94] However since then it has been shown that folding is a more general collapse mechanism. Yet, it must be stressed that the folding mechanism is very sensitive to experimental conditions, and is not always reversible. In some cases changes in temperature, compression rate, or subphase composition either eliminate folding or cause the folding

mechanism to facilitate the formation of lipid vesicles, tubes, or micelles.[91,94,101] These structures are ejected into the subphase and the collapse is therefore irreversible. In order for folding to be reversible, the film must be neither too rigid nor too fluid.

For films composed of a mixture of lipids, the collapse pressure, $\pi_c$, determines whether a miscible mixture has formed. If a binary mixture is miscible the $\pi_c$ of the mixture has typically a value intermediate between those of the pure components. Typically if mixed monolayers are immiscible, a "squeezing out" of the component with the lower collapse pressure is observed. This can be seen in the $\pi$-A isotherm as a plateau or decrease in surface pressure at the $\pi_c$ of the lower component, followed by an increase in surface pressure until the collapse of the second component.[80,102] Imaging techniques can also assist with determining miscibility, by observing the corresponding collapse structures.[103]

## 2.2 Brewster Angle Microscopy

Brewster angle microscopy is an imaging technique based on the reflection of p-polarized light at the Brewster angle on an aqueous subphase. On neat water, little reflection of light occurs at the Brewster angle. However, once a monolayer has been spread of the water surface, the refractive index of the surface has changed and increased reflection now occurs.[104] BAM provides morphological information similar to fluorescence microscopy, but has the advantage that a probe molecule is not needed.[105] In the following sections the basic notions of polarization, as well as reflection and refraction of light will be discussed.

### 2.2.1 Plane Harmonic Waves

Light is a form of electromagnetic (EM) radiation at a wavelength λ that behaves as a wave as it propagates in a medium (Figure 2.3). The wave is composed of electric field (**E**) and magnetic field (**H**) vectors, which oscillate in phase perpendicular to each other and maintain a fixed ratio of intensities. If the oscillation of both **E** and **H** is perpendicular to the direction of propagation as described by **k**, the propagation vector, then the wave is a transverse wave. Furthermore the transverse wave can be described as a plane-harmonic wave if **E** oscillates sinusoidally in time and is constant over an infinite set of planes that are perpendicular to the direction of propagation. A plane harmonic wave can be mathematically represented as

$$\boldsymbol{E}(\boldsymbol{r}, t) = E_0 e^{i(\boldsymbol{kr}-\omega t)} \tag{2.25}$$

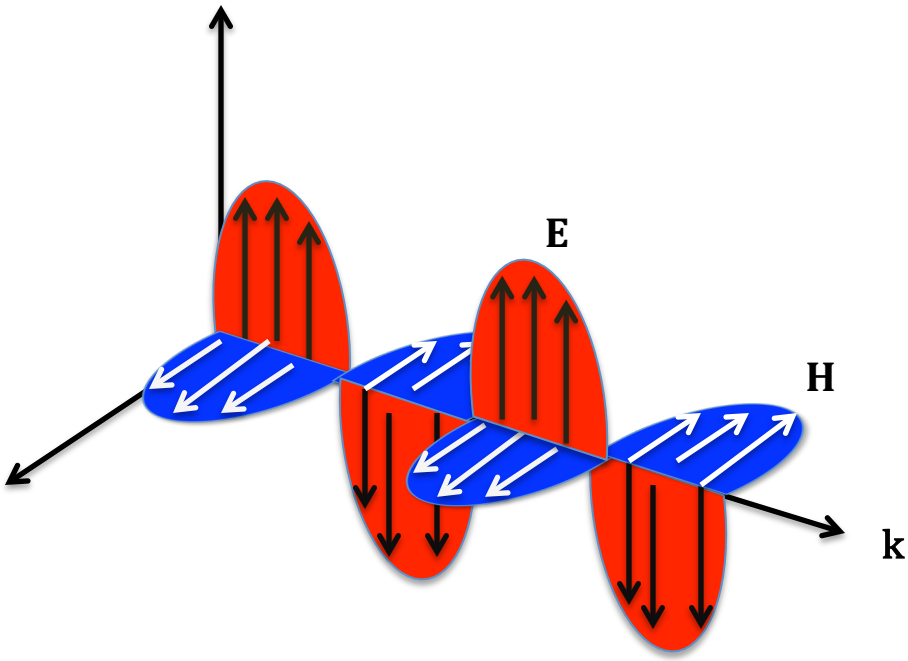


**Figure 2.3.** Schematic diagram of an electromagnetic wave

where $E_0$ is the amplitude of the wave, **r** is the position vector, and ω is the angular frequency of the wave.[106,107]

### 2.2.2 Polarization States

Polarized light results from the oscillation of the electric field in a fixed plane. The process of creating polarized light is known as polarization, where the direction of polarization is determined from the direction of electric field. A polarized electric field can be resolved into two mutually perpendicular components, $\mathbf{E}_1$ and $\mathbf{E}_2$. These orthogonal components are often denoted as the parallel ($\mathbf{E}_p$) or perpendicular ($\mathbf{E}_s$)

components to the surface plane, and are more commonly referred to as *p*- or *s*-polarized components. Superposition of these two orthogonal components leads to polarization, where three different states of polarization can be adopted: linear, circular or elliptical. The state of polarization depends upon the amplitude and phase of the combined waves.

For instance, if the waves have a phase difference of 0° or ± 360° the waves are in the same plane, resulting in a combined wave in that same plane with an amplitude that is the sum of the amplitudes of the individual components. The resultant electric field is restricted to a single, linear plane, and is therefore linearly polarized. Circular and elliptical polarizations arise from the combination of orthogonal waves that are out of phase. In the case of circularly polarized light, this phase difference is 90°, and results in an electric field that traces a circle. Circular polarization has the constraint that the two waves must have the same amplitude. Otherwise a difference in amplitudes or a phase difference between 0° and 90° produce elliptically polarized light.[106–108]

### 2.2.3 Reflection and Refraction of Light

When a plane harmonic wave impinges at an incident angle $\theta_i$ upon a boundary between two mediums, $M_1$ and $M_2$, of differing refractive indices, $n_1$ and $n_2$, part of the wave is reflected, part is absorbed, and part is refracted. It will be assumed in this discussion that both media are dielectric, and therefore that absorption does not occur. The reflected wave is generated in $M_1$ at an angle $\theta_r$, and the refracted wave propagates through $M_2$ at an angle $\theta_t$. A schematic diagram of these processes can be seen in Figure 2.4.

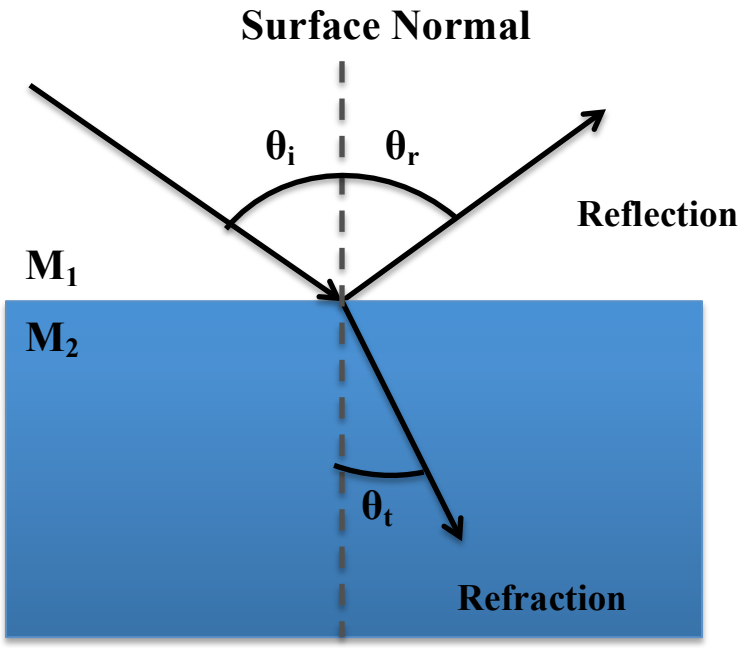


**Figure 2.4.** Reflection and refraction of a plane-harmonic wave

The Maxwell equations stipulate that boundary conditions be upheld, in which the tangential components of the electric field are continuous as the boundary is crossed. This can mathematically be represented as

$$\boldsymbol{E_i} + \boldsymbol{E_r} = \boldsymbol{E_t} \tag{2.26}$$

where $\boldsymbol{E}_i$, $\boldsymbol{E}_r$, and $\boldsymbol{E}_t$ are the incident, reflected, and refracted electric fields, respectively. These electric fields can be represented similar to Eq. (2.25).

$$\boldsymbol{E_i}(\boldsymbol{r}, t) = E_{0i} e^{i(\boldsymbol{k_i}\cdot\boldsymbol{r} - \omega t)} \tag{2.27}$$

$$\boldsymbol{E_r}(\boldsymbol{r},t) = E_{0r}e^{i(\boldsymbol{k_r}\cdot\boldsymbol{r}-\omega t)} \quad (2.28)$$
$$\boldsymbol{E_t}(\boldsymbol{r},t) = E_{0t}e^{i(\boldsymbol{k_t}\cdot\boldsymbol{r}-\omega t)} \quad (2.29)$$

The propagation vector, **k**, can be further broken down into incident, reflected, and refracted wave vectors

$$\vec{k_i} = k_i(sin\theta_i\hat{\boldsymbol{x}} - sin\theta_i\hat{\boldsymbol{y}}) \quad (2.30)$$
$$\vec{k_r} = k_r(sin\theta_r\hat{\boldsymbol{x}} + sin\theta_r\hat{\boldsymbol{y}}) \quad (2.31)$$
$$\vec{k_t} = k_t(sin\theta_t\hat{\boldsymbol{x}} - sin\theta_t\hat{\boldsymbol{y}}) \quad (2.32)$$

For a constant relationship to exist for all points of the boundary, the exponential functions Eq. (2.27)-(2.29) must be equal for all values of time, i.e.

$$k_i sin\theta_i = k_r sin\theta_r = k_t sin\theta_t \quad (2.33)$$

Since the incident and reflected waves propagate in the same medium the wave vectors are the same, and therefore the incident and reflected angles are equivalent.

$$\theta_i = \theta_r \quad (2.34)$$

This is Snell's first law. If it is considered that $k = n/c$, then the relationship between the incident and reflected waves can be expressed as

$$n_1 sin\theta_r = n_2 sin\theta_t \quad (2.35)$$

This is Snell's second law.

The amplitude ratios of the reflected or refracted waves with respect to the incident wave can be used to determine the fraction of reflected and refracted light, and are given by the Fresnel equations.

$$r_s = \frac{E_{0rs}}{E_{0is}} = -\frac{sin(\theta_i - \theta_t)}{sin(\theta_i + \theta_t)} \quad (2.36)$$

$$r_p = \frac{E_{0rp}}{E_{0ip}} = -\frac{tan(\theta_i - \theta_t)}{tan(\theta_i + \theta_t)} \quad (2.37)$$

$$t_s = \frac{E_{0ts}}{E_{0is}} = \frac{2cos\theta_i sin\theta_t}{sin\,(\theta_i + \theta_t)} \quad (2.38)$$

$$t_p = \frac{E_{0tp}}{E_{0ip}} = \frac{2cos\theta_i sin\theta_t}{sin\,(\theta_i + \theta_t)cos\,(\theta_i - \theta_t)} \quad (2.39)$$

where *r* and *t* are the reflected and refracted amplitude ratios, respectively, and the subscripts *s* and *p* denote the *s* and *p* components of the electric field.

The reflectance is the fraction of the incident light that is reflected, and is proportional to the square of the reflected amplitude ratio. The reflectance can be determined for both the *s* and *p* components

$$R_s = |r_s|^2 = \left|\frac{E_{0rs}}{E_{0is}}\right|^2 \quad (2.40)$$

$$R_p = |r_p|^2 = \left|\frac{E_{0rp}}{E_{0ip}}\right|^2 \quad (2.41)$$

The amount of reflected or refracted light is dependent upon the angle of incidence and the polarization of light, as can be seen from the Fresnel equations.

### 2.2.4 Brewster Angle

At a specific angle of incidence the amplitude ratio of reflected *p*-polarized light approaches zero. Looking at Eq. (2.37) it can be seen that this results when $\theta_i + \theta_t = 90°$. The angle of incidence at which this phenomenon occurs is known as the Brewster angle, $\theta_B$, and can be calculated from Snell's law of refraction.

$$n_1 sin\theta_i = n_2 sin(90 - \theta_i) = n_2 cos\theta_i \quad (2.42)$$

or

$$\theta_B = tan^{-1}\left(\frac{n_2}{n_1}\right) \quad (2.43)$$

For example, the refractive indices of air and water are 1 and 1.33, respectively, therefore the Brewster angle for the air-water interface is 53.1°.

### 2.2.5 Factors that Influence the Intensity of Reflected Light

The intensity of reflected light is dependent upon many factors, mainly the thickness and roughness of the interface, and anisotropy of monolayers.[109] Ideally the *p*-polarized reflectance at the neat air-water interface at the Brewster angle is practically zero ($\leq 10^{-8}$). The scenario of zero (or minimal) reflection has the conditions that the interface is smooth and that the refractive index changes abruptly from one medium to another. However, for a real interface the reflectance has a slightly higher value due surface roughness and the fact that the refractive indices do not change abruptly.

Reflectance is also affected by the optical anisotropy of monolayers. Anisotropy of monolayers increases reflectance. The orientation of molecules influences the reflectivity, as can be seen by the greater reflectivity of condensed monolayers.[109]

# Chapter 3 Materials and Methods

## 3.1 Materials

Cholesterol and palmitic acid were obtained from Sigma Aldrich with purities of 98% and 99%, respectively. Bovine galactocerebrosides (Bcerebrosides) with a purity of >97% was purchased from Sigma Aldrich and used without any further purification. Porcine cerebrosides (Pcerebrosides) was obtained from Avanti Lipids, Inc. with a purity of >99% and used without further purification. Stock solutions were prepared using chloroform and methanol (HPLC grade, Fisher Scientific). Monolayers were spread on a pure water subphase with a resistivity of 18.0 MΩcm (Barnstead nanopure filtration system) and a measured pH of 5.6. All experiments were completed at room temperature (22 ± 1°C) and atmospheric pressure.

## 3.2 Methods

### 3.2.1 Sample Preparation

Stock solutions of cholesterol and PA were prepared by dissolution of solid powder in chloroform. Solutions of Bcerebrosides and Pcerebrosides were made by dissolution of solid powders in a chloroform/methanol mixture with a 1:1 (v/v) ratio.

The Bcerebrosides sample used in these experiments is a mixture of Type I and Type II galactocerebrosides with varying chain lengths. Type I and Type II categorize the fatty acid chains of the cerebroside, where Type I contains α-hydroxy fatty acid (HFA), and Type II contains non-hydroxy fatty acid (NFA) chains. Since the amounts and types of cerebrosides in the mixture were not specified an exact molecular weight could not be used to calculate molecular areas. A procedure similar to that of Johnston was used to determine an average molecular weight.[110] It was assumed that a 50/50 mixture of HFAs and NFAs was present. The most predominant NFA in bovine brain has a molecular weight of 796 g/mol.[110] 32 g/mol was added to this weight for the α-hydroxyl substituted chains, and the average weight of 812 g/mol was used in sample preparation.

The Pcerebrosides sample is also a mixture of HFAs and NFAs. NFA chains were more abundant and the composition of NFAs can be found in Table 3.1. An average molecular weight of 781.953 g/mol was used for calculating molecular concentrations.

**Table 3.1**. Nonhydroxylated fatty acid composition in porcine cerebrosides

| Chain | % of Total Lipids |
|---|---|
| 16:0 | 6 |
| 18:0 | 7 |
| 20:0 | 3 |
| 22:0 | 11 |
| 24:0 | 22 |
| 24:1 | 9 |

### 3.2.2 π-A Isotherms

π-A isotherms were obtained using a KSV minitrough (KSV Instruments, Finland). The Teflon trough has dimensions of 168 mm × 85 mm. Symmetric compression of the monolayer is completed using two barriers coated with Delrin, a hydrophilic material. Surface pressure and mean molecular area (MMA) were monitored during compression by the Wilhelmy plate method. Filter paper (Ashless grade, Whatman) served as the Wilhelmy plate. Prior to each experiment the trough was cleaned thoroughly with ethanol and rinsed several times with ultrapure water. The trough was then filled with ultrapure water. To check for impurities the subphase was swept with the barriers to ensure that no significant rise in surface pressure (≤ 0.2 mN/m) was observed during compression. A measured amount of lipid solution was then spread dropwise on the subphase using a microsyringe (Hamilton), and 10 minutes was allowed for solvent evaporation after spreading. The barriers were compressed at a constant rate of 5mm/min/barrier.

### 3.2.3 BAM Imaging

BAM images were measured simultaneously with π-A isotherms on a custom built setup. The setup consists of a goniometer, which provides the framework for all other optical and mechanical components, a sample stage, and a black plastic box. Attached to the goniometer are two arms, where one arm supports all components relevant to emission, including the laser source, a half-wave plate (HWP) and a polarizer. The components necessary for detection are found on the other arm and include an

objective lens, a tube lens, and a charged couple device (CCD) camera. Some of these optical components will be discussed in further detail in the following sections. The incident angle of these arms is controlled by the goniometer and can be varied in the range 40-60 degrees. The goniometer also allows the height of these arms to be adjusted. The sample stage is a vertically adjustable lab jack with an area large enough to support the Langmuir trough. A flat black glass plate rests upon a Teflon wedge at the bottom of the trough, and serves to absorb any refracted light. The inclination of the plate also prevents any remaining light from reaching the detector. A black Plexiglass box with two frontal mobile doors covers the whole setup to protect it from air currents and dust as well as to minimize ambient parasitic light. Most final images were cropped from the full 800 μm × 800 μm image to show the most resolved areas in the image. No further image processing was done.

*Laser Source*

A HeNe laser (Research Electro-Optics) is used as light source. The laser emits highly *p*-polarized light (>500:1) at 543 nm with a maximum output power of 5 mW.

*Half-Wave Plate and Polarizer*

The output light from the laser source was first attenuated by a HWP (Ekspla, Lithuania) with an anti-reflective coating at 532 nm. Further filtration of the output light is done by a Glan prism (Ekspla, diameter 14 mm) with a coating that is antireflective in the range 430-960 nm.

*Objective Lens and Tube Lens*

An infinity-corrected Nikon CF objective lens is used in this BAM setup. It has a linear magnification of 10×, a working distance of 20.3 mm, and a numerical aperture of 0.21. The objective lens is mounted on two micrometer stages so that the *x* and *y* axes can be adjusted accordingly. Used along with the objective lens is a tube lens (MXA22018, Nikon). The tube lens has a focal length of 200 mm and focuses the collimated light from the objective lens into the CCD.

*CCD Camera*

BAM images were captured on a back-illuminated electron multiplying CCD camera (DV887-BV, Andor Technology). The CCD has 512 × 512 active pixels. Each pixel has a size of 16 μm × 16 μm resulting in a total image area of 8.2 mm × 8.2 mm. Andor Solis software along with a CCl-22 PCI controller card were used for image acquisition. 14 bit megapixel images were recorded with pixel read out rates of 10, 5, 3, or 1 MHz.

# Chapter 4 Results and Discussion

## 4.1 Surface Pressure-Area Isotherms

### 4.1.1 Cholesterol, Palmitic Acid, Bovine Cerebrosides, and Porcine Cerebrosides

The phase behavior of Langmuir monolayers are described by π−Area isotherms.[80] Figures 4.1-4.4 show the π−Area isotherms of pure cholesterol, pure PA, Bcerebrosides, and Pcerebrosides. The phase behavior of cholesterol and PA have been well documented.[80,111–113] Isotherms of mixtures of bovine HFA and NFA Bcerebrosides have only been previously reported once.[114] Several reports of individual isotherms of bovine HFAs and NFAs exist and were used for comparison. [3,110,114–116] To the best of the author's knowledge, π−Area isotherms of porcine cerebrosides have not been reported. Reports of Bcerebrosides were used for comparison.

In Figure 4.1, following the isotherms from right to left along the MMA axis, a sharp increase in surface pressure of the cholesterol monolayer can be seen at 38 $Å^2$/molecule. This indicates a transition from the gas-liquid-condensed (G-LC) coexistence phase to a purely liquid-condensed (LC) phase. The presence of a G-LC coexistence phase at 0 mN/m is evident from BAM images and will be discussed further

in Section 4.2.1. Film collapse occurs at 45 mN/m and at a MMA of 35 Å$^2$/molecule. The brevity of the LC phase suggests that molecules are rigidly packed and the alkyl chains are perpendicular to the water surface. Results found here are consistent with those previously reported.[111,112,117–120]

The isotherm of PA can be seen in Figure 4.2. Results reported here are consistent with previous studies.[113,121,122] The G-LC to LC transition (evidenced by BAM) occurs at 26 Å$^2$/molecule. A kink at 25 mN/m indicates a molecular reorganization and has previously been attributed to a second-order transition from a tilted condensed (TC) phase to an untilted condensed (UC) phase.[93,121,123] Therefore, two LC phases exist in the isotherm, and the G-LC to LC transition is actually the G-TC to TC transition. Collapse of the monolayer occurs at 40 mN/m.

The Bcerebrosides monolayer begins to increase in surface pressure at 40 Å$^2$/molecule (Figure 4.3). The film has a fluid-like transition with no discontinuities, indicating a G-LC to LC transition (evidenced by BAM). A lack of obvious collapse is observed, which may be due to the formation of a bilayer.[114] Variation in the collapse pressure occurred, and ranged from 52-55 mN/m. In comparison to previous works of HFA and NFA monolayers the shape of the Bcerebrosides mixture isotherm is in good agreement with those of HFAs and sometimes with NFAs.[110,114,115] The Bcerebrosides isotherm obtained here differs from the one reported by Johnston in that the G-LC occurs at smaller MMAs, and a discontinuity at low pressures is not observed. However, Johnston noted that mixed films of HFAs and NFAs have large variability in the area at which surface pressure increases, resulting in two distinct isotherms for the same

mixture.[114] Therefore differences in the MMA of the G-LC to LC transition may be due to variability in the phase behavior of Bcerebrosides. As noted earlier, the exact composition of fatty acid chains in the Bcerebrosides mixture used here is not known, and may be a contributing factor. The discontinuity observed by Johnston is most likely due to differences in experimental temperatures. It has been shown that an increase in temperature leads to a discontinuity in the isotherm of galactocerebrosides.[9] Variations in HFA/NFA content, fatty acid chain composition, and experimental parameters may be the reason for the observed differences. Generally, though, the shape of the cerebrosides isotherm reported here matches those of previous works.

In Figure 4.4, the G-LC to LC transition (evidenced by BAM) of Pcerebrosides occurs at 38 $Å^2$/molecule. Similar to the Bcerebrosides monolayer, the transition is fluid and lacks discontinuities. The surface pressure steadily increases until approximately 50 mN/m, where the collapse phase begins. Variability in the onset of collapse was observed, and typically ranged between 50-60 mN/m. After this point the surface pressure still increases, but at a much slower pace. Overall the shape is very similar to that of Bcerebrosides, but Pcerebrosides are able to reach a higher surface pressure than Bcerebrosides when compressed to the same MMA.

### 4.1.2 Mixed Monolayers of Cholesterol and Bovine Cerebrosides

As mentioned earlier, one of the aims of this investigation is to study the miscibility and organization of mixed films of cholesterol and cerebrosides. Figure 4.5 shows the isotherms of mixtures with varying ratios of cholesterol and Bcerebrosides. No

distinct trend can be observed for the overall series, indicating that cholesterol does not have a condensing effect on Bcerebrosides. This differs from previous reports on the interactions of cholesterol and Bcerebrosides, in which cholesterol did have a condensing effect, but the difference in behavior may be due to experimental conditions.[114,124] For example, Johnston had an experimental temperature of 37°C, while Nakahara used an aqueous NaCl subphase. It is expected that the interactions of these molecules behave differently with changes in temperature and subphase composition.

Marked differences in phase behavior can be observed depending upon the cholesterol content, as seen in Figures 4.5-4.10. A large variability in the π-A isotherm of the 1:10 mixture was observed. Therefore the isotherm that was most reproducible is represented in Figure 4.6. The MMA at which the G-LC to LC transition occurred was always greater than that of pure Bcerebrosides, indicating that an expansion of the monolayer occurred. Expansion of the monolayer suggests that repulsive interactions are dominant in the low surface pressure regime. Fluid-like behavior similar to that of pure Bcerebrosides was observed, however the compressibility varied greatly, in which the MMA occupied by mixtures varied for the same surface pressure. Leveling off of the surface pressure or a change in the slope of the isotherm was typically observed at 50 mN/m.

Expansion of the monolayer is also observed for the 1:1 mixture. Transition from G-LC to LC occurs at 41 $Å^2$/molecule. The 1:1 mixture occupies a larger molecular area than the pure Bcerebrosides until leveling off of surface pressure occurs at 41 mN/m. This suggests that repulsive forces dominate for the entirety of the isotherms. The 1:3 and

2:1 mixtures both have G-LC to LC transitions at 40 $Å^2$/molecule. Both have fluid-like behavior, but the 2:1 mixture occupies a larger molecular area throughout the isotherm. Collapse pressures occur at 42 and 40 mN/m, respectively. The 4:1 mixture is unique in that it is the only isotherm in the series to show a discontinuity. The G-LC to LC transition is at 39 $Å^2$/molecule, followed by a change in slope in the isotherm at 37 $Å^2$/molecule. This suggests that a reorientation of molecules occurs at this point. After this point the isotherm maintains a constant slope until collapse at 40 mN/m.

Notable for all mixtures is that no distinct collapse is observed. The collapse phase for all mixed films resembles that of Bcerebrosides, in which the surface pressure either levels off or very slowly increases after reaching a limiting molecular area. Collapse pressures were assigned to the pressure at which leveling off occurred, and can be seen in Figure 4.11. Solid lines indicate the collapse pressures of pure cholesterol and Bcerebrosides monolayers. Two points at $\chi_{Chol} = 0$ show the range of collapse pressures observed for Bcerebrosides monolayers. The collapse pressure varies for all mixtures, but generally the mixtures had lower collapse pressures than pure cholesterol. This suggests that the mixed monolayers were less stable than the pure components. However, the fact that collapse pressures varied from the pure components indicates that all mixtures form miscible monolayers. If the mixtures were immiscible a "squeezing out" of cholesterol, which has the lower collapse pressure, would be observed. Typically, mixtures are immiscible if a collapse at the surface pressure of the less stable component is observed, followed by an increase in surface pressure to the collapse pressure of the more stable component. However, an increase in surface pressure is not observed for any mixed

cholesterol/Bcerebroside films after the initial collapse pressure, even when compressed to small molecular areas, thus suggesting their miscibility.

Miscibility of mixed films can also be determined from the additivity rule.[80,102]

$$A_{12} = \chi_1 A_1 + \chi_2 A_2 \quad (4.1)$$

The additivity rules states that at a specific surface pressure the MMA of a mixed film, $A_{12}$, is related to the molecular area and mole fraction of the pure components, $\chi_1$ and $\chi_2$. If the two components obey the additivity rule the film is immiscible or behaves ideally. Therefore any deviation from the additivity rule indicates miscibility and non-ideal behavior. Plots of $A_{12}$ vs. $\chi_{Chol}$ for Bcerebrosides/cholesterol mixtures are shown in Figure 4.12. In the low surface pressure regime positive deviations were observed, indicating that the interaction of the cholesterol and Bcerebrosides molecules are weaker than between each component with itself. However, as surface pressure increased negative deviations can be seen for some mole fractions. For both the mid and high surface pressure regimes negative deviations occur for $\chi_{Chol} \leq 0.33$ and $\chi_{Chol} \geq 0.8$. This suggests that at higher surface pressures the composition of mixed film determines whether repulsive or attractive forces dominate. Overall, though, based on the additivity rule, all mixtures of cholesterol and cerebroside presented here are miscible.

The stability of the mixed monolayers can be determined from the excess free energy of mixing, $\Delta G_{ex}$, and the free energy of mixing, $\Delta G_{mix}$. For a mixed monolayer at constant surface pressure and temperature the expression for $\Delta G_{ex}$ is

$$\Delta G_{ex} = \int_0^{\pi} [A_{12} - (x_1 A_1 + x_2 A_2)] d\pi \quad (4.2)$$

where $\pi$ is surface pressure. The $\Delta G_{mix}$ can be determined from the relationship

$$\Delta G_{mix} = \Delta G_{ex} + \Delta G_{ideal} \quad (4.3)$$

where $\Delta G_{ideal}$ can be calculated based on experimental conditions,

$$\Delta G_{ideal} = RT(x_1 ln x_1 + x_2 ln x_2) \quad (4.4)$$

where R is the gas constant and T is the temperature. Using the Eq. (4.2), the $\Delta G_{ex}$ and for various cholesterol/cerebrosides mixtures was calculated and is shown in Figure 4.13. Positive and negative values are seen in the $\Delta G_{ex}$. Negative values imply attractive interactions between cholesterol and cerebroside, while positive values imply repulsive interactions. From the $\Delta G_{ex}$ plot it can be see that repulsive interactions are dominant in the range $0.33 \leq \chi_{chol} \leq 0.8$, while outside this range attractive interactions dominate.

Figure 4.14 shows a plot of $\Delta G_{mix}$ as a function of mole fraction of cholesterol. Values are negative for all monolayer compositions, indicating the mixed monolayers were thermodynamically more stable than pure cholesterol or Bcerebrosides. Negative values also imply that the monolayers are in fact miscible mixtures.

### 4.1.3 Mixed Monolayer of Cholesterol and Porcine Cerebrosides

Figure 4.15 shows the isotherms of a 1:1 mixture of Pcerebrosides and cholesterol. The mixture is more compressible than both pure components. The G-LC to LC transition occurs at 37 $Å^2$/molecule. Surface pressure increases steadily until 44 mN/m, where the surface pressure levels off for the remainder of the isotherm. Only one collapse pressure is observed, suggesting miscibility between Pcerebrosides and cholesterol. Comparison of the 1:1 mixtures of Pcerebrosides/cholesterol and Bcerebrosides/cholesterol shows similar phase behavior, as the shape of isotherms is match. However, the Bcerebroside/cholesterol mixture is expanded compared to the pure components while the Pcerebrosides/cholesterol mixture is compressed compared to the pure components. This suggests that while Pcerebrosides and Bcerebrosides behave similarly, Pcerebrosides and Bcerebrosides have, respectively, attractive and repulsive interactions with cholesterol.

Differences in behavior of porcine and bovine cerebrosides may be attributed to fatty acid chain composition. The headgroup, galactose, did not vary between these two molecules. Fatty acid composition for both cerebrosides is not completely known, but it is expected that some variation in the abundance of certain chain lengths between the two cerebrosides occurs. Previous studies on mixed films of cholesterol and fatty acids have shown that changes in fatty acid chain length can influence the phase behavior.[117] Therefore it is expected that differences in fatty acid chain composition between porcine and bovine cerebrosides would also affect the phase behavior of the mixtures, as van der Waal interactions in the two films would differ.

### 4.1.4 Mixed Monolayers of Palmitic Acid and Porcine Cerebrosides

Figures 4.16 - 4.20 shows isotherms of mixtures of PA and Pcerebrosides with varying ratios. From Figure 4.16 it can be seen that isotherms of mixtures generally lay between that of the pure components, which suggests that PA has a condensing effect on Pcerebrosides. The exception to this is the 4:1 mixture, which is slightly more compressible than pure PA. A change in phase behavior can be observed between the 3:2 and 2:3 mixtures. The 4:1 and 3:2 mixtures have similar phase behavior, and the 1:4 and 2:3 mixtures have similar phase behavior. However different phase behavior is found between the the two pairs of mixtures. Both the 4:1 and 3:2 mixtures have G-LC to LC transitions at approximately 26 $Å^2$/molecule. Two LC phases are present, in which a kink occurs at 15 mN/m for both mixtures. The collapse phase also occurs at the same surface pressure, 51 mN/m, for these mixtures, However, only one LC phase is observed for the 1:4 and 2:3 mixtures, and their collapse phases are at lower surface pressures, at 41 and 44 mN/m, respectively.

Notable for the 1:4 and 2:3 mixtures is that the surface pressure begins increasing at a molecular area larger than that of pure Pcerebrosides. For the 4:1 mixture this occurs at 47 $Å^2$/molecule. The surface pressure slowly increases to about 2 mN/m until 36 $Å^2$/molecule, where the surface pressure rapidly increases. Similarly, for the 2:3 mixture, the surface pressure begins increasing at 46 $Å^2$/molecule until it reaches a value of 2 mN/m at 30 $Å^2$/molecule, where the it then rapidly increases. The expansion of these

monolayers indicates that repulsive interactions occur in the low-pressure regime, and that a LE phase may exist for these two mixtures.

Overall, the presence of one collapse phase for each mixture indicates that mixtures of PA and Pcerebrosides are miscible. Collapse pressures were assigned to the surface pressure in which leveling off occurred, and can be seen in Figure 4.21. Two points at $\chi_{PA} = 0$ show the range of collapse pressures observed for Pcerebrosides. Values were between those of the pure components. The decrease in collapse pressure as Pcerebrosides content increases suggests that stability of the mixed films is dependent upon composition. "Squeezing out" of PA was not observed for any mixture, even on compression to relatively small molecular areas. The presence of two LC phases in the 4:1 and 3:2 mixtures suggests that they are more like PA in their behavior, while the 1:4 and 2:3 mixtures are more like Pcerebrosides in behavior.

Thermodynamic analysis similar to that of cholesterol/Bcerebrosides mixtures was also done for Pcerebrosides/PA mixed films. Figure 4.22 shows a plots of $A_{12}$ vs. $\chi_{PA}$ at 5, 20, and 35 mN/m. In the low-pressure regime positive deviations are observed for $\chi_{PA} = 0.2$. For $\chi_{PA} > 0.2$, negative deviations are seen and indicate attractive interactions between Pcerebrosides and PA molecules. At higher surface pressures, negative deviations are observed with the exception of $\chi_{PA} = 0.2$, which exhibits near ideal behavior.

The variations in $\Delta G_{ex}$ for various compositions of Pcerebrosides and PA are shown in Figure 4.23. Values for $\Delta G_{ex}$ are all negative with the exception of $\chi_{PA} = 0.2$ at 5 and 20 mN/m. This indicates that interactions between Pcerebrosides and PA are

mostly attractive. The values of $\Delta G_{ex}$ become more negative with increasing surface pressure, suggesting that the mixed monolayer is more stable at higher surface pressures. This may be due to stronger interactions between molecules as the monolayer is condensed. A minimum in the $\Delta G_{ex}$ values can be seen in each curve at $\chi_{PA} = 0.6$, indicating that this composition is the most thermodynamically stable.

Figure 4.24 shows the $\Delta G_{mix}$ for Pcerebrosides/PA mixtures. All values of $\Delta G_{mix}$ are negative, indicating that mixed films of Pcerebrosides and PA are miscible. Therefore the interactions between Pcerebrosides and PA molecules are attractive and stronger than the interactions of pure components with themselves.

As mentioned earlier, it was observed that PA has a condensing effect of Pcerebrosides. Such an effect may be due to hydrogen-bonding betweent the different headgroups. PA has a carbonyl headgroup, and cerebrosides have a galactose with several hydroxyl groups. The carbonyl group of PA may serve as a bridging structure, in which hydroxyl groups from neighboring galactose groups preferentially hydrogen bond to the carbonyl group instead with neighboring water molecules. Such behavior would result in closely packed headgroups, as the solvation shell of the galactose is now replaced with PA carbonyl groups. Van der Waals interactions most likely also help facilitate condensation, as alkyl chains of similar length and structure could easily pack together.

## 4.2 BAM Images

### 4.2.1 Cholesterol, Palmitic Acid, Bovine Cerebrosides, and Porcine Cerebrosides

Figures 4.25-4.28 show images of pure cholesterol, palmitic acid, Bcerebrosides, and Pcerebrosides monolayers during compression. Cholesterol domains can be seen in the gas phase, even at large surface pressures. The domains are circular and typically small, however, large circular domains have also been observed. As the G-LC MMA is approached domains begin to fuse together until a fully condensed phase forms. White aggregates begin forming at surface pressures as low as 20 mN/m. After the collapse surface pressure has been reached small white aggregates are seen. As the monolayer is compressed further these aggregates grow in number and size. The results obtained here match those previously reported.[47,119]

BAM images of a PA monolayer are shown in Figure 4.26. Domains are visible at relatively large surface areas, indicating coexistence of G-TC phases. Shapes of the domains vary, appearing as wide shapeless condensed areas, or as small circular shapes. Domains fuse near the G-TC transition point, i.e. 26 $Å^2$/molecule. Formation of white bulky aggregates can be seen at surface pressures of 17 mN/m or greater. The size and brightness of the aggregates grow after the collapse point is reached. Results obtained here agree well with those previously reported.[47,97,122,125]

Bcerebrosides monolayers have a condensed-like phase that is visible at surface areas as large as 80 $Å^2$/molecule. Domains do not have any specific shape or structure, but are typically large enough to take up the whole field of view of the objective lens. Little change is observed in surface morphology until the collapse phase is reached.

Formation of line-like structures begins at 46 mN/m. These structures may appear as bright white aggregates, as can be seen in panel 6 of Figure 4.27, or as a line shape within the condensed phase, as can be seen in panels 7-8. Results reported here for the G-LC coexistence region differ from a previous report on BAM images of bovine galactocerebrosides.[126] BAM images of Bcerebrosides showed asymmetrical, wire-shaped domains. However, the author describes the domains as rigid clusters with irregular boundaries, which is consistent with results reported here. Differences in visual appearance of the domains in the G-LC coexistence phase may be due experimental conditions or fatty acid composition of the Bcerebrosides. The condensed phase reported here is consistent with literature. BAM images of the collapse phase of Bcerebrosides monolayers have not been previously reported. However, electron micrographs have shown that long, narrow structures form in the collapse phase of ceramide galactosides, which is consistent with collapse structures reported here.[127]

Pcerebrosides are very similar to Bcerebrosides in their surface morphology. At large surface areas bright, irregularly shaped condensed-like phases are observed. Little change in the morphology is seen until a surface pressure of approximately 55 mN/m, when the brightness of the condensed phase reduces, and a crosshatched-like pattern is observed. A reduction of brightness in the film suggests partial solubilization of the monolayer into the subphase.[95] With continued compression bright, line-shaped structures appear and grow in numbers, as can be seen in panels 7-8 in Figure 4.28.

### 4.2.2. Mixed Monolayers of Cholesterol and Bovine Cerebrosides

Figure 4.29 shows BAM images for a 1:10 mixed monolayer composition. At large surface areas condensed-like phases similar to that of cerebrosides are seen. White spots are visible in all images; however, the cause of these white spots is unknown. A fully condensed monolayer forms after 42 $Å^2$/molecule. After this point the brightness of the image increases with increasing compression. Collapse of the monolayer occurs at 50 mN/m, but no distinct change in morphology occurs. At 20 $Å^2$/molecule, the appearance of dark areas suggests that some of the monolayer has been lost to the subphase during compression.

BAM images of a 1:3 mixed monolayer can be seen in Figure 4.30. At large surface areas domains do not have any specific shape. Domains may be seen with large irregular voids, small circular voids, or line-shaped voids, as is evident in panels 1-3 in Figure 4.30. As the G-LC to LC transition is neared, a fully condensed phase forms. Upon collapse of the film, small white aggregates begin to form. As compression to smaller molecular areas is continued the number of aggregates grows rapidly, as can be seen in the last panel of Figure 4.30.

Figure 4.31 shows images for a 1:1 mixture. Domains appear as a condensed phase with circular or donut-shaped voids at large molecular areas. Even after the G-LC to LC transition, these circular voids may be present until higher surface pressures. After collapse small white aggregates form. The number of these aggregates increases and decreases corresponding, respectively, to rises and falls in the $\pi-A$ isotherm, but

generally the number of white aggregates at the end of compression is less than all collapse due to a slight decrease in surface pressure.

The 2:1 mixture has similar domain appearance as the 1:1 at large surface areas, as can be seen in Figure 4.32. A condensed phase with circular or donut-shaped voids can be seen. However, line-shaped voids may also be present. White aggregates may form at the collapse pressure, but they are usually not numerous. Like the 1:1 mixture, increase and decrease in the numbers of white aggregates correspond to increase and decreases in surface pressure, respectively. In the images shown here, a small number of aggregates are present at 20 $Å^2$/molecule due a decrease in surface pressure.

BAM images of the 4:1 mixture are shown in Figure 4.33. At large surface areas domains appear as a condensed phase with shapeless or line-shaped voids, as can be seen in panels 1-4. After the G-LC to LC transition a web-like condensed phase forms. Upon collapse white aggregates form. With continued compression the white aggregates continue to grow, but in the web-like pattern observed in the condensed phase.

From the five cholesterol/Bcerebrosides mixtures discussed above, variation in the collapse structure of the mixture was observed depending upon the chemical composition of the mixture. While some collapse structures were similar to those of pure cholesterol, the white aggregates seen in mixtures did not grow into the rod-like shapes of pure cholesterol when compressed to small molecular areas. This suggests that a new collapse phase differing from pure cholesterol was formed, also indicating that cholesterol and Bcerebrosides are miscible. Furthermore, the collapse structure of Bcerebrosides, the line-shaped structure, was not observed in any BAM images for

mixtures, indicating that “squeezing out” of cholesterol did not occur. Therefore the BAM images for cholesterol/Bcerebrosides mixture support the conclusion that miscible mixed films have been formed.

### 4.2.3 Mixed Monolayer of Cholesterol and Porcine Cerebrosides

Figure 4.34 shows BAM images of a 1:1 mixture of cholesterol and Pcerebrosides. At large molecular areas domains similar to that of pure Pcerebrosides are visible. The domains do not have any distinct shape and small circular or donut-like voids can be seen in the condensed domains. At surface pressures greater than 0 mN/m the circular voids are no longer observed. At the collapse point, at around 40 mN/m, formation of small white aggregates occurs. Continued compression results in rapid growth in the number of aggregates, as can be seen in panels 6-7 in Figure 4.34.

Compared to the 1:1 cholesterol/Bcerebrosides mixture, many similarities are observed. Both these mixtures have domains shaped similar to the pure cerebrosides, respectively. Circular or donut-like voids can be seen in the condensed domains. The main difference between the two mixtures is the collapse phase. While both form white aggregates, the cholesterol/Bcerebrosides mixture has a decrease in the number of aggregates on the surface due to a decrease in the surface pressure. In contrast, the cholesterol/Pcerebrosides mixture does not have a decrease in surface pressure, and therefore the numbers of aggregates grow with compression. Otherwise, the surface morphology of the 1:1 mixtures is rather similar, suggesting that Bcerebrosides and Pcerebrosides have similar interactions with cholesterol.

It was earlier discussed in Section 4.1.3 that van der Waals interactions influence the phase behavior for mixtures of cholesterol and cerebrosides. Despite difference in fatty acid chain composition, BAM images reveal that the surface morphology of 1:1 mixtures of porcine/cholesterol and bovine/cholesterol are similar for all phases. Such an observation suggests that headgroup interactions are more dominant than van der Waal interactions. Hydrogen bonding of galactose headgroups may be stronger than alkyl chain interactions, which may lead to the similarities in surface morphology.

### 4.2.4 Mixed Monolayers of Palmitic Acid and Porcine Cerebrosides

Shown in Figure 4.35 are BAM images for a 1:4 mixture of PA and Pcerebrosides. At large surface areas the domains appear similar to those of pure Pcerebrosides, in that they have no distinct shape. Domains have a foam-like appearance, as many small holes are visible. After the G-LC to LC transition the small holes disappear and a fully condensed monolayer is formed. After the collapse point, 40 mN/m, no change in morphology of the monolayer is observed. A condensed phase is observed even at small molecular areas, 15 $Å^2$/molecule, as can be seen in the last panel of Figure 4.35. However, line-shaped structures on the condensed phase are sometimes observed at small molecular areas (not shown here).

Figure 4.36 shows images of a 2:3 mixture. The domains have no distinct shape at large surface areas, and small holes may be seen in the films. Upon compression a fully condensed monolayer forms at 30 $Å^2$/molecule. At smaller molecular areas, e.g. 20

Å$^2$/molecule, line-shaped structures begin to form. One or several lines may be visible. However, line-shaped collapse structures are not always observed, although.

BAM images for a 3:2 mixture are presented in Figure 4.35. At large molecular areas domains appear similar to pure cerebrosides (not shown), and may have large unshapely voids. Formation of a fully condensed monolayer does not occur until after the G-LC to LC transition at 26 Å$^2$/molecule. Similar to the 1:4 and 2:3 mixtures, line-shaped structures may or may not be visible at molecular areas smaller than 20 Å$^2$/molecule.

Figure 4.36. show BAM images of a 4:1 mixture. Domains are shapeless and appear similar to Pcerebrosides at large molecular areas. A fully condensed monolayer forms after 26 Å$^2$/molecule. At 40 mN/m, formation of bulky white aggregates occurs. However, further compression of the monolayer results in formation of web-like pattern that resembles neither pure PA nor pure Pcerebrosides.

Comparison of the four mixtures reveals that similar surface morphologies are observed for the 1:4, 2:3, and 3:2 mixtures. A condensed phase was formed that sometimes resulted in line-shaped collapse structures. While this collapse structure resembles that of Pcerebrosides, the collapse structure of PA was not observed during the course of the isotherm compression, indicating that the collapse structure formed here is a new collapse structure unique to the mixtures.

The 4:1 mixture differed most in its surface morphology. Formation of bulky, white aggregates began close to or at the collapse pressure of PA. However, a decrease in surface pressure was not observed in the π-A isotherm, suggesting a “squeezing out” of PA does not occur. The formation of white aggregates later gives way to formation of a

web-like structure on the surface. Line-shaped collapse structures were never observed for the 4:1 mixture. Although the bulky white aggregates resemble the collapse structure of PA, a lack of "squeezing out" and the absence of the line-shaped collapse structure of Pcerebrosides indicate that this is a new collapse structure unlike the pure components. Therefore, mixtures of PA and Pcerebrosides are miscible due to the formation of new collapse structures.

BAM images shown here also support the condensing effect observed in π-Area isotherms in section 4.1.4. All mixed films show similarity in surface morphology to a degree, whether it be in the G-LC, LC, or C phases. Round domains typical of PA are not observed in any films, and films appear very similar to that of pure Pcerebrosides. This suggests that the galactose headgroup is the dominant factor in determining surface morphology. As discussed previously, hydrogen bonding between PA and Pcerebrosides headgroups may be favorable, which may result in a surface structure that resembles Pcerebrosides.

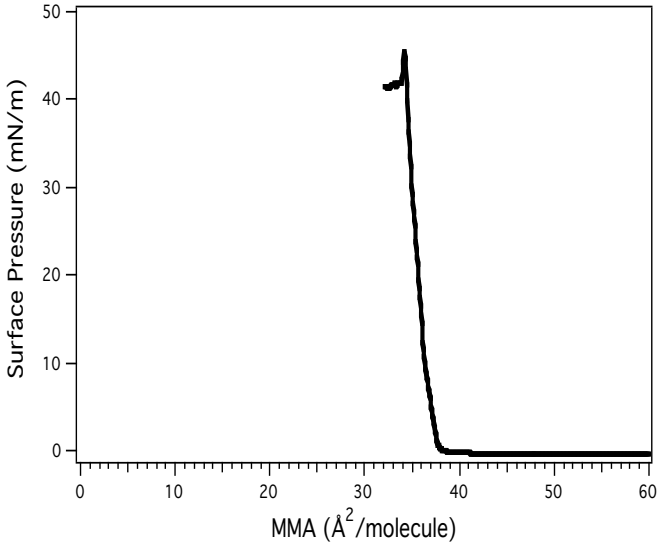


**Figure 4.1.** π–Area isotherm of cholesterol monolayer on ultrapure water

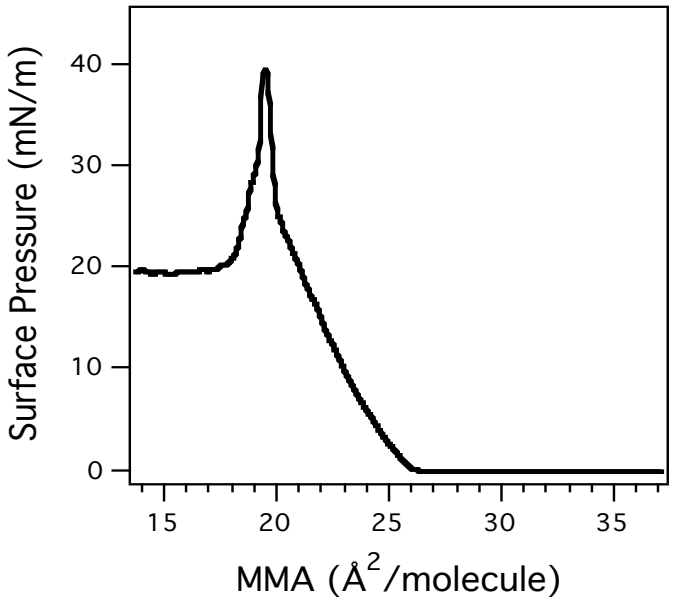


**Figure 4.2.** π-Area isotherm of palmitic acid monolayer on ultrapure water

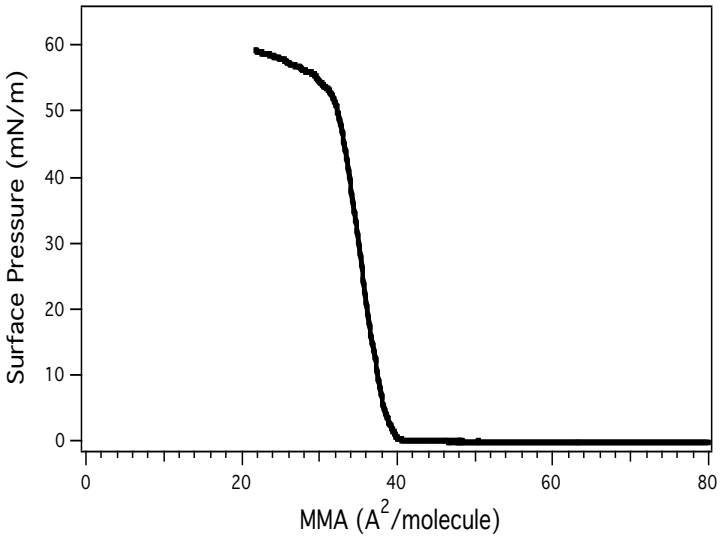


**Figure 4.3.** π –Area isotherm of bovine cerebrosides monolayer on ultrapure water

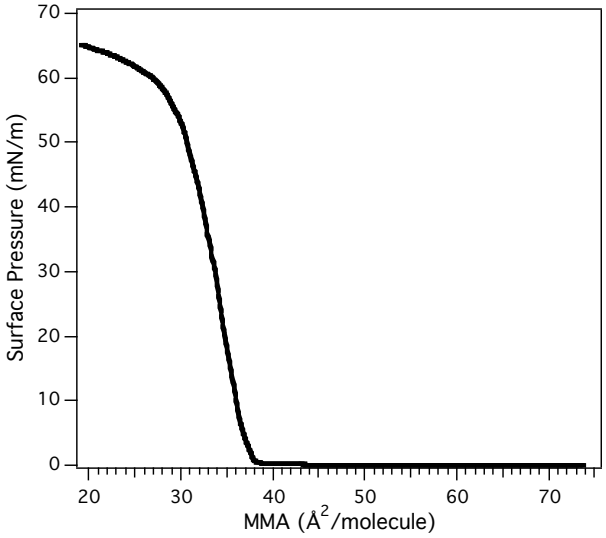


**Figure 4.4.** π –Area isotherm of porcine cerebrosides monolayer on ultrapure water

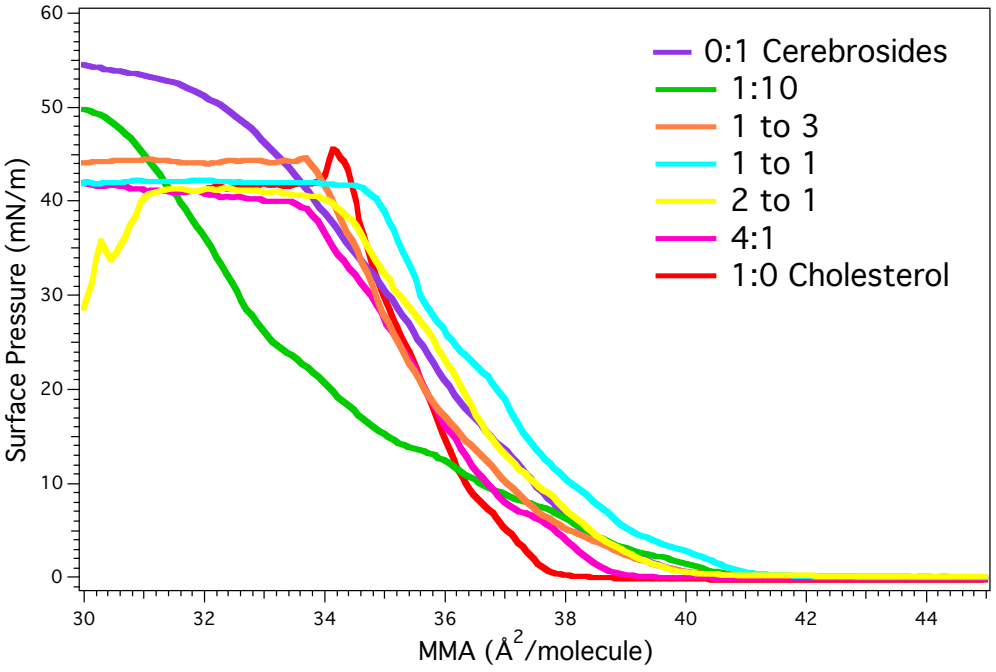


**Figure 4.5.** π-Area isotherms of cholesterol/bovine cerebrosides mixed monolayer with various ratios on ultrapure water

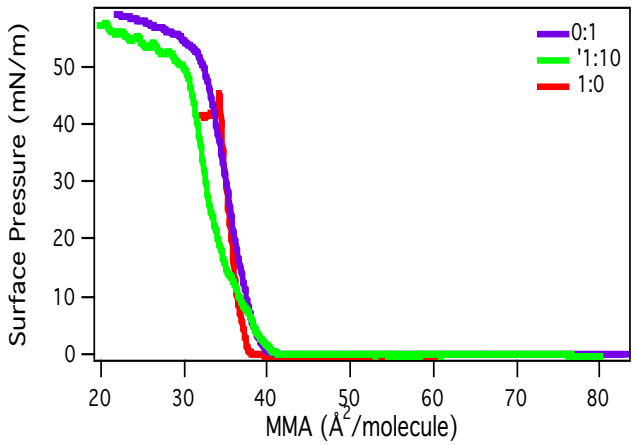


**Figure 4.6.** π-Area isotherm of a 1:10 cholesterol/bovine cerebrosides mixed monolayer on ultrapure water

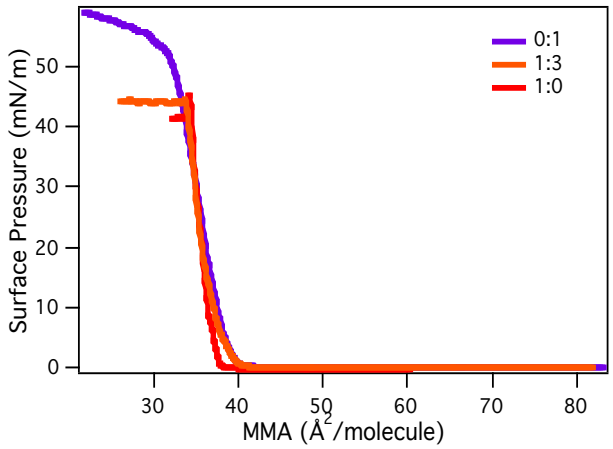


**Figure 4.7.** π-Area isotherm of a 1:3 cholesterol/bovine cerebrosides mixed monolayer on ultrapure water

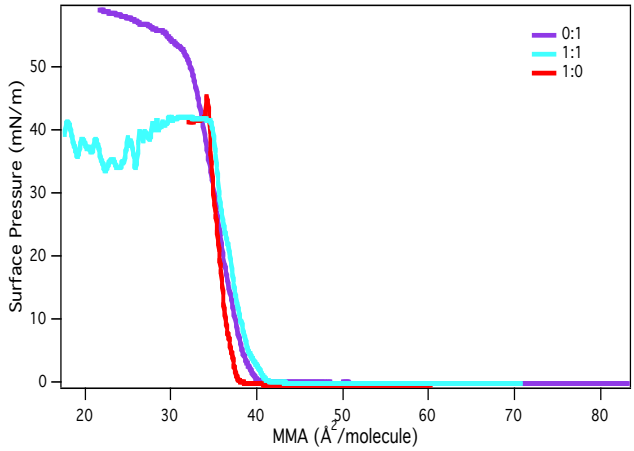


**Figure 4.8.** π-Area isotherm of a 1:1 cholesterol/bovine cerebrosides mixed monolayer on ultrapure water

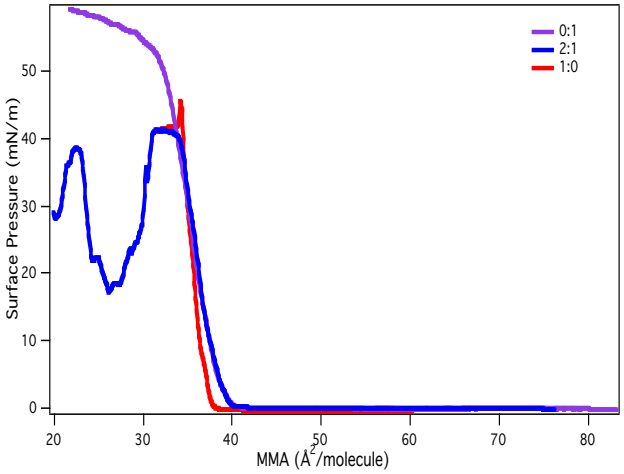


**Figure 4.9.** π-Area isotherm of a 2:1 cholesterol/bovine cerebrosides mixed monolayer on ultrapure water

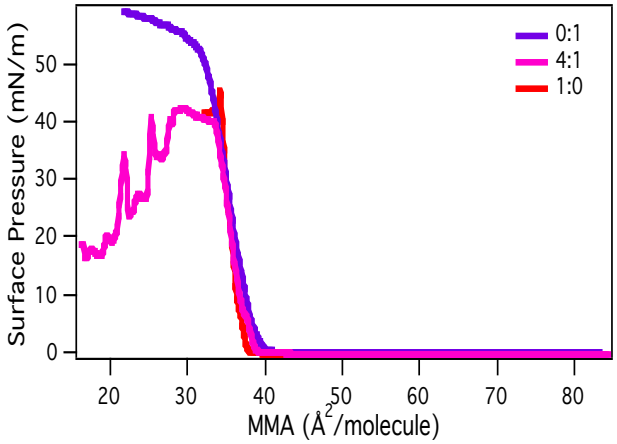


**Figure 4.10.** π-Area isotherm of a 4:1 cholesterol/bovine cerebrosides mixed monolayer on ultrapure water

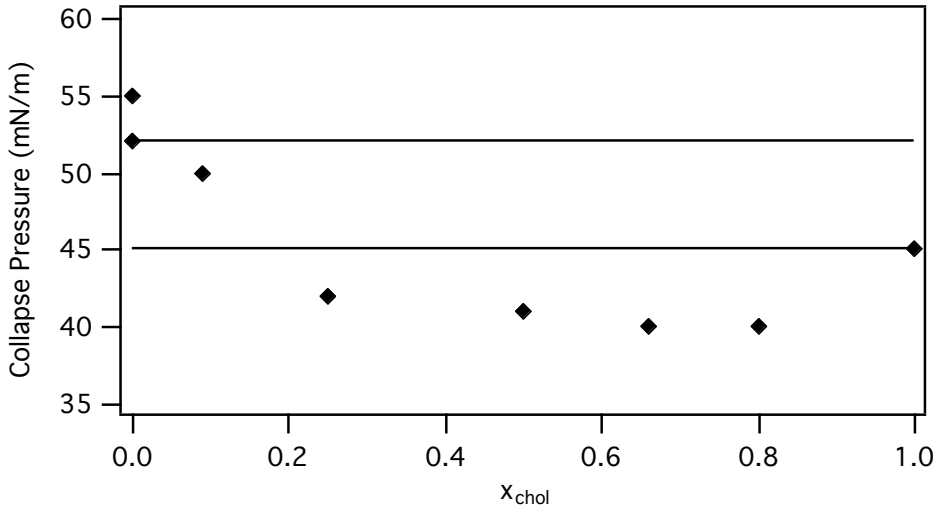


Figure 4.11. Collapse pressures of cholesterol/bovine cerebrosides mixtures as a function of cholesterol chemical composition.

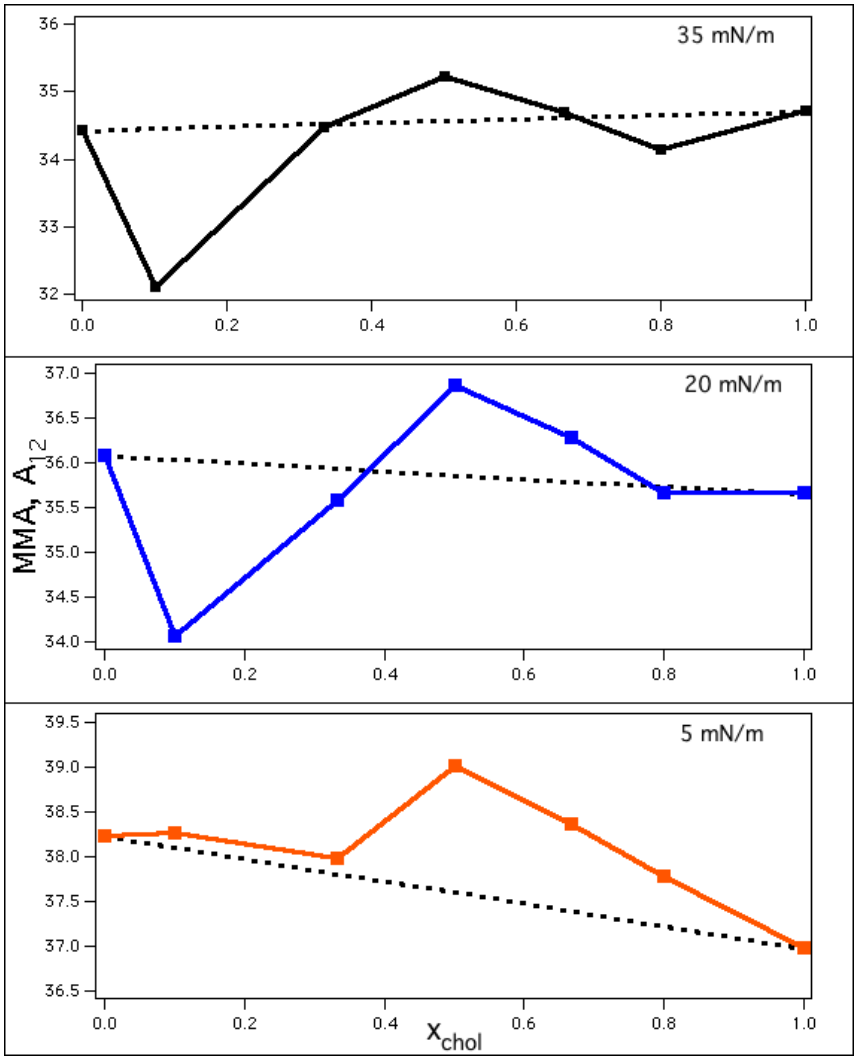


**Figure 4.12.** MMA of cholesterol/bovine cerebrosides mixtures as function of cholesterol chemical composition at various surface pressures

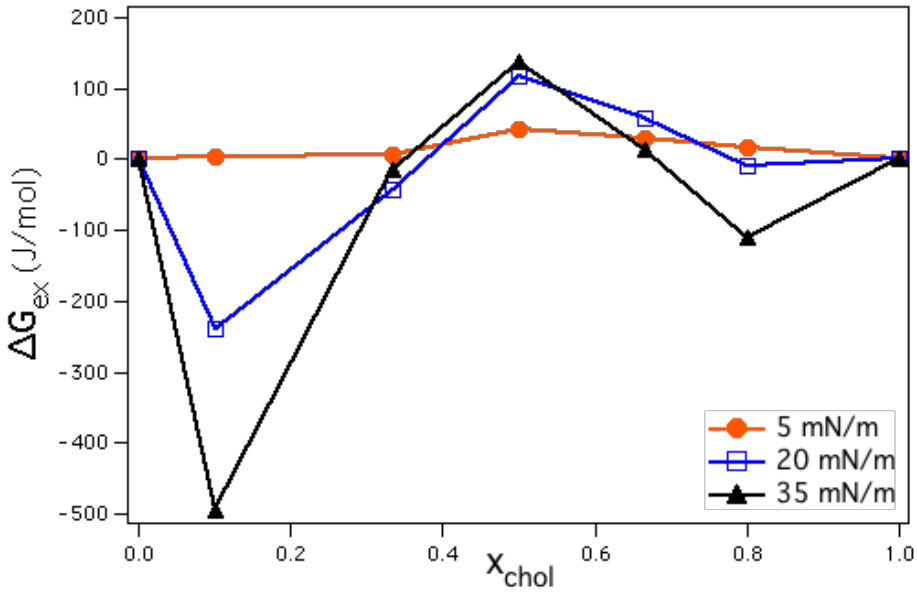


**Figure 4.13.** Excess free energies of mixing of cholesterol/bovine cerebrosides mixtures as a function of cholesterol chemical composition at various surface pressures.

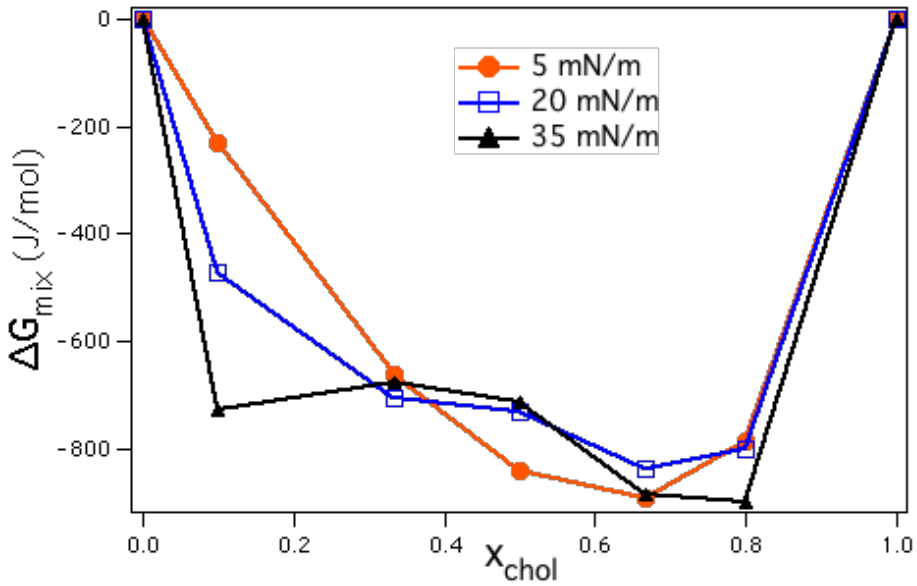


**Figure 4.14.** Free energies of mixing of cholesterol/bovine cerebrosides mixtures as a function of cholesterol chemical composition at various surface pressures.

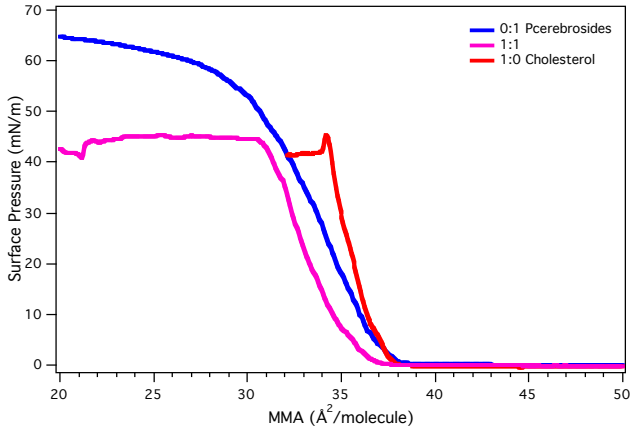


**Figure 4.15.** π-Area isotherm of a 1:1 cholesterol/porcine cerebrosides mixed monolayer on ultrapure water

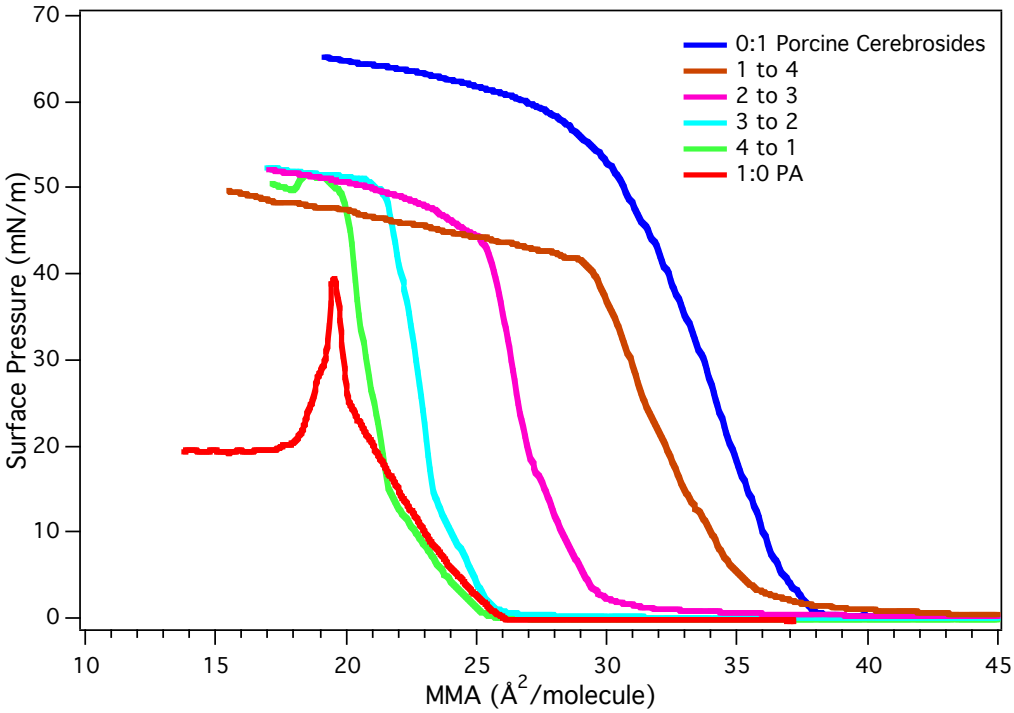


**Figure 4.16.** π -Area isotherms of palmitic acid/porcine cerebrosides mixed monolayer with various ratios on ultrapure water

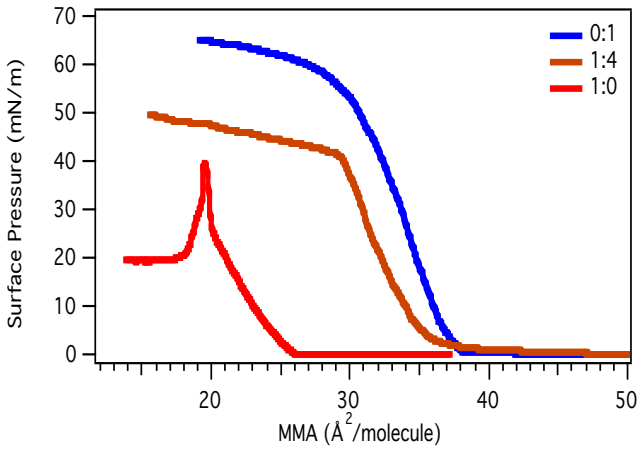


**Figure 4.17.** π -Area isotherm of 1:4 palmitic acid/porcine cerebrosides monolayer on ultrapure water

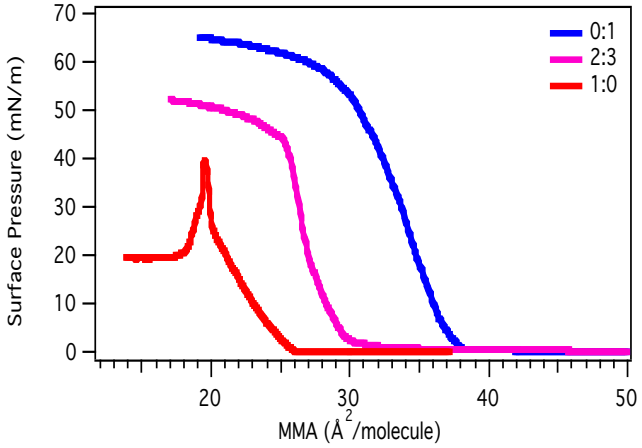


**Figure 4.18.** π -Area isotherm of 2:3 palmitic acid/porcine cerebrosides mixed monolayer on ultrapure water

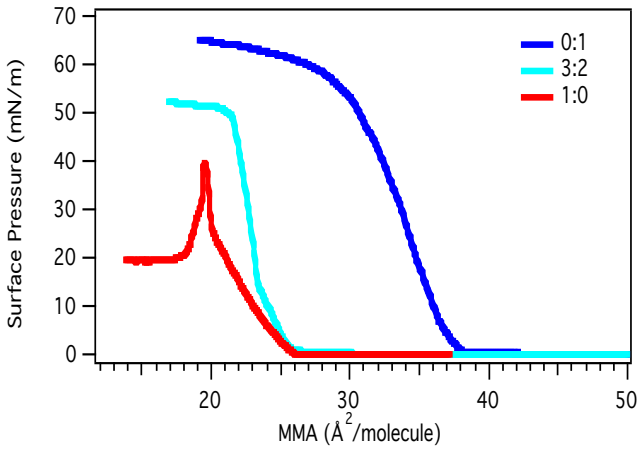


**Figure 4.19.** π -Area isotherm of 3:2 palmitic acid/porcine cerebrosides mixed monolayer on ultrapure water

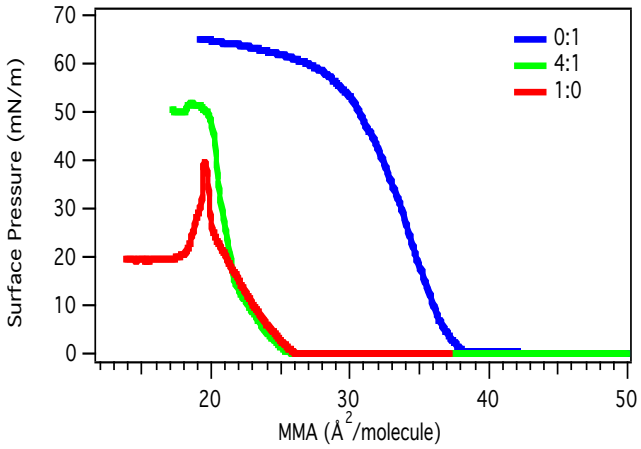


**Figure 4.20.** π -Area isotherm of 4:1 palmitic acid/porcine cerebrosides mixed monolayer on ultrapure water

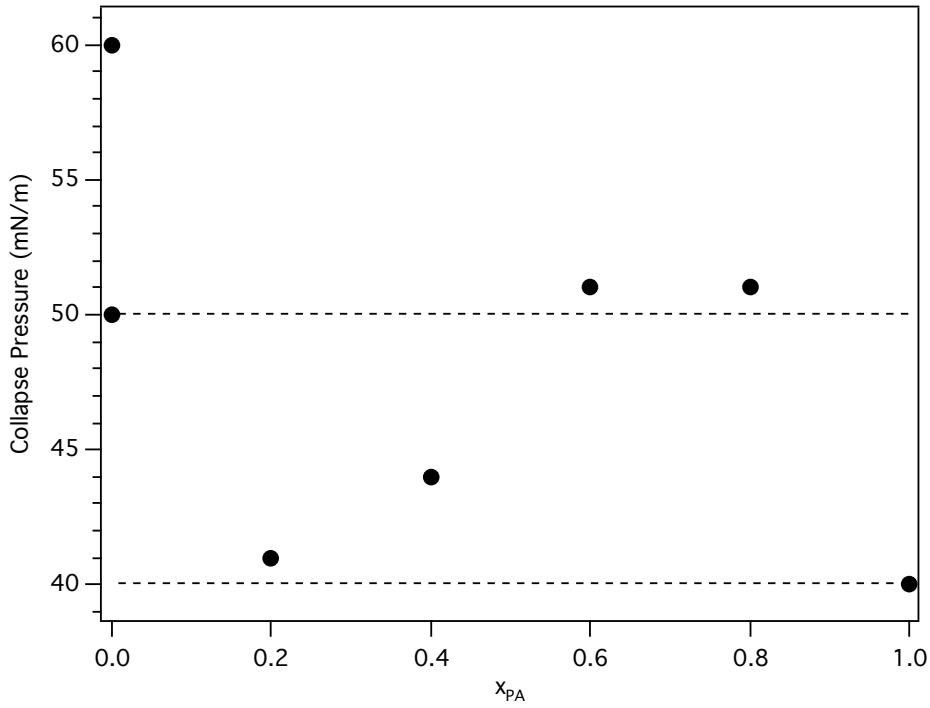


**Figure 4.21.** Collapse pressures of palmitic acid/porcine cerebrosides mixed monolayers as a function of palmitic acid chemical composition.

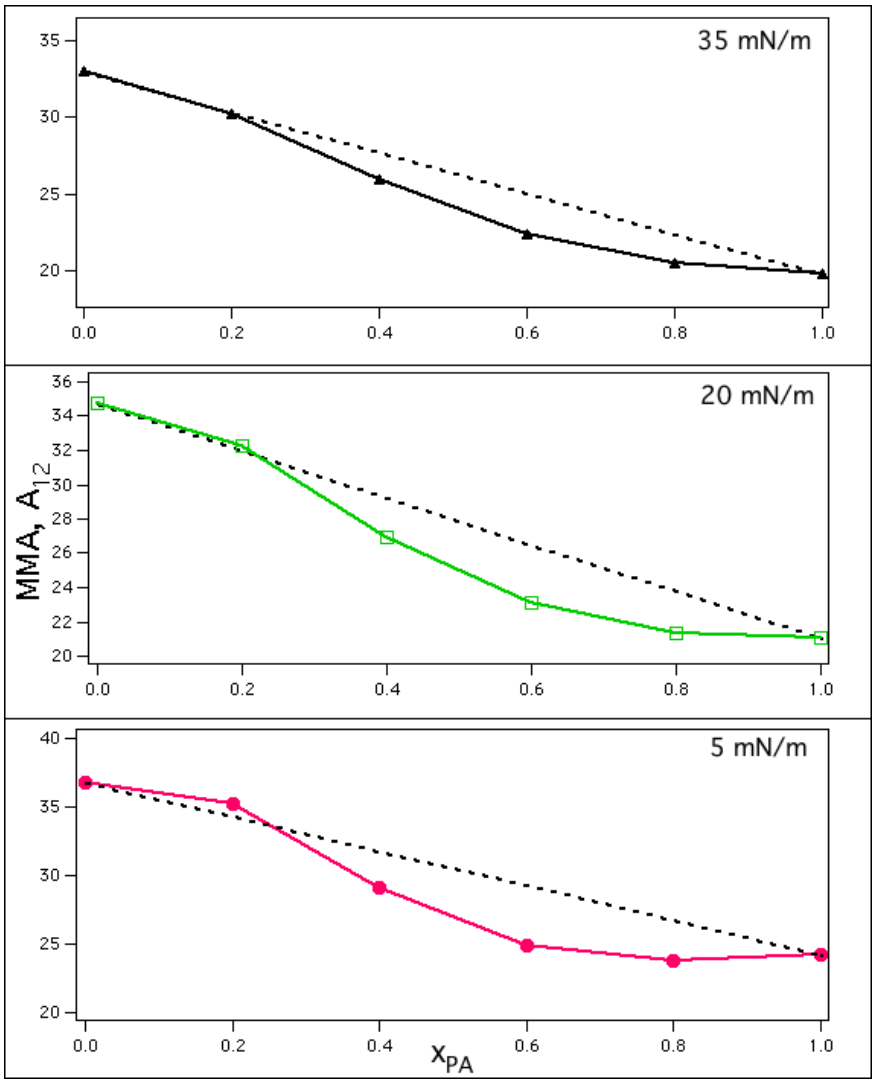


**Figure 4.22.** Mean molecular areas of palmitic acid/porcine cerebrosides mixtures as a function of palmitic acid chemical composition at various surface pressures.

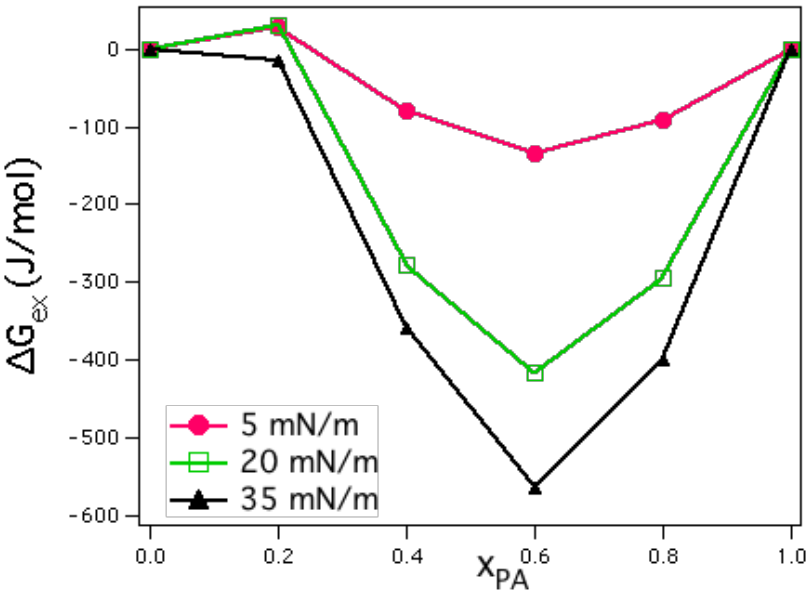


**Figure 4.23.** Excess free energies of mixing of palmitic acid/porcine cerebrosides mixtures as a function of palmitic acid chemical composition at various surface pressures

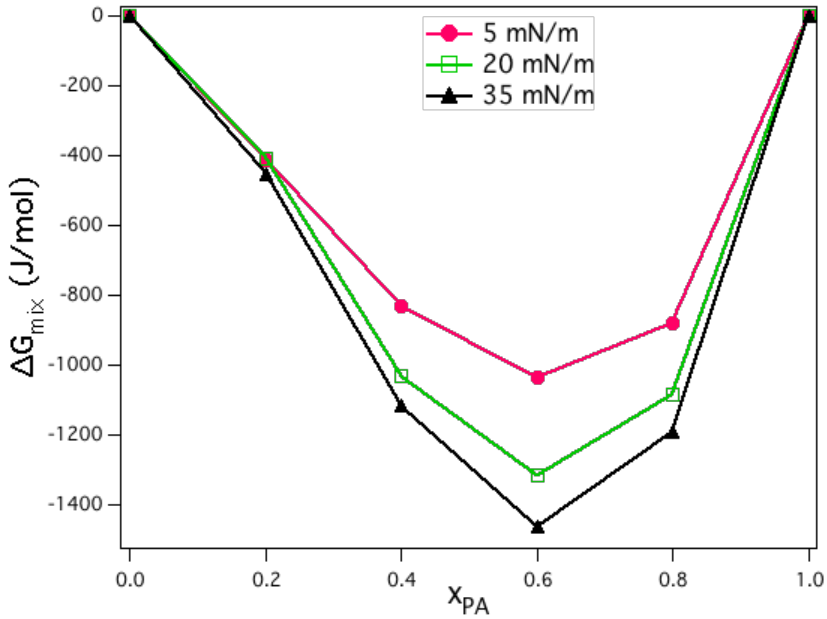


**Figure 4.24.** Free energies of mixing of palmitic acid/porcine cerebrosides mixtures as a function of palmitic acid chemical composition at various surface pressures.

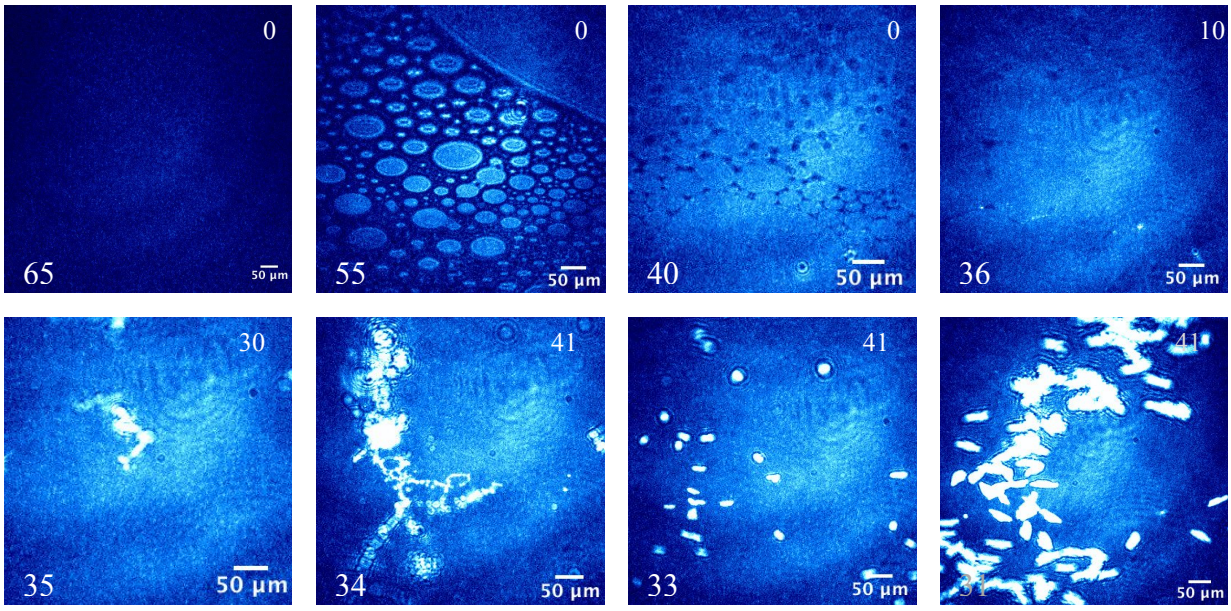


**Figure 4.25.** BAM images cholesterol monolayer during compression. Numbers in the top right are surface pressures, while numbers in the bottom left are corresponding molecular areas

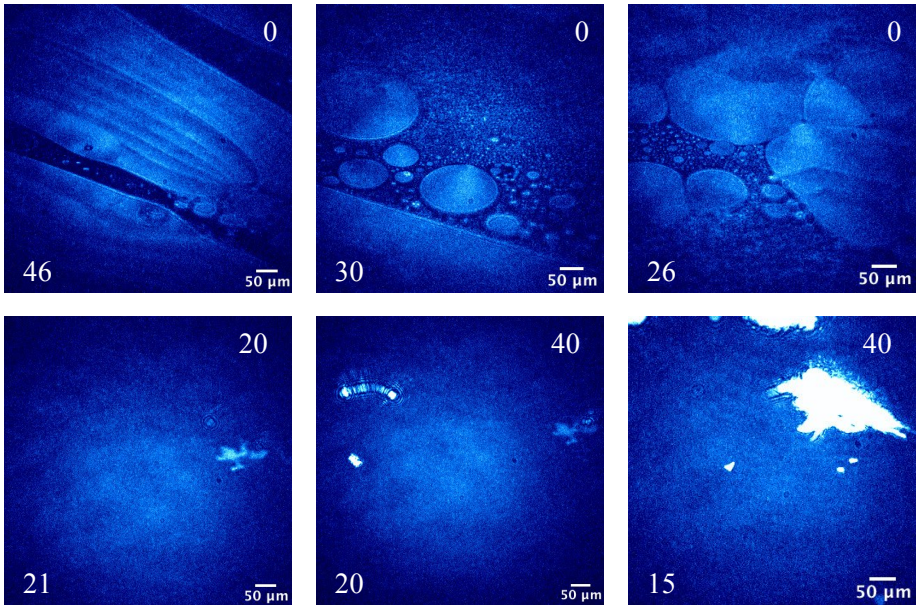


**Figure 4.26.** BAM images of palmitic acid monolayer during compression.

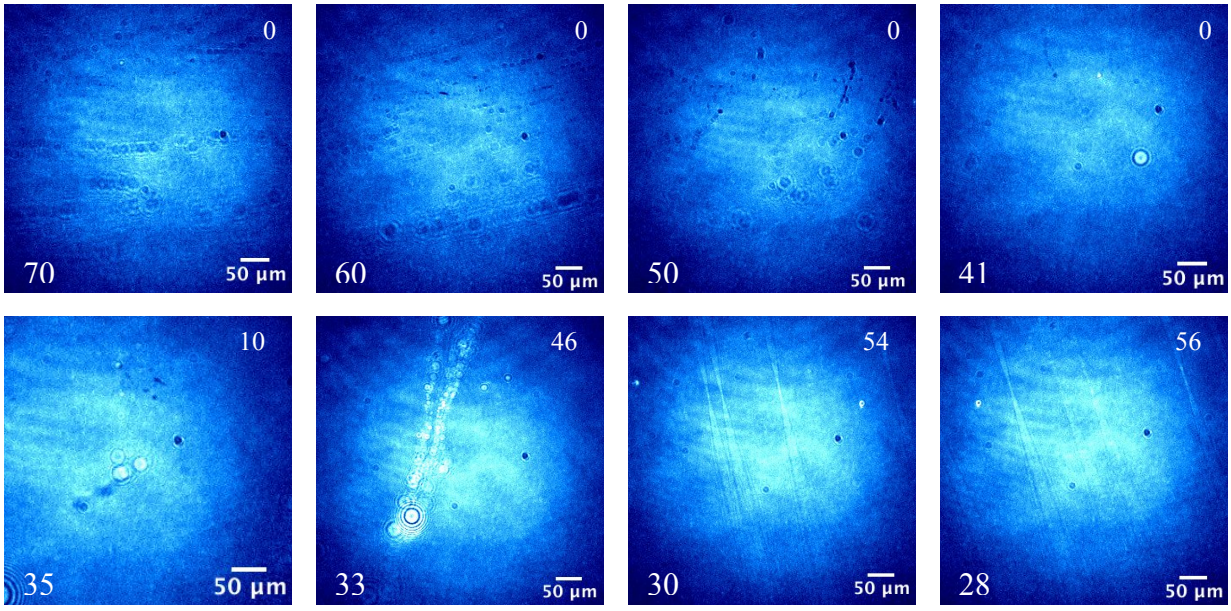


**Figure 4.27.** BAM images of bovine cerebrosides monolayer during compression.

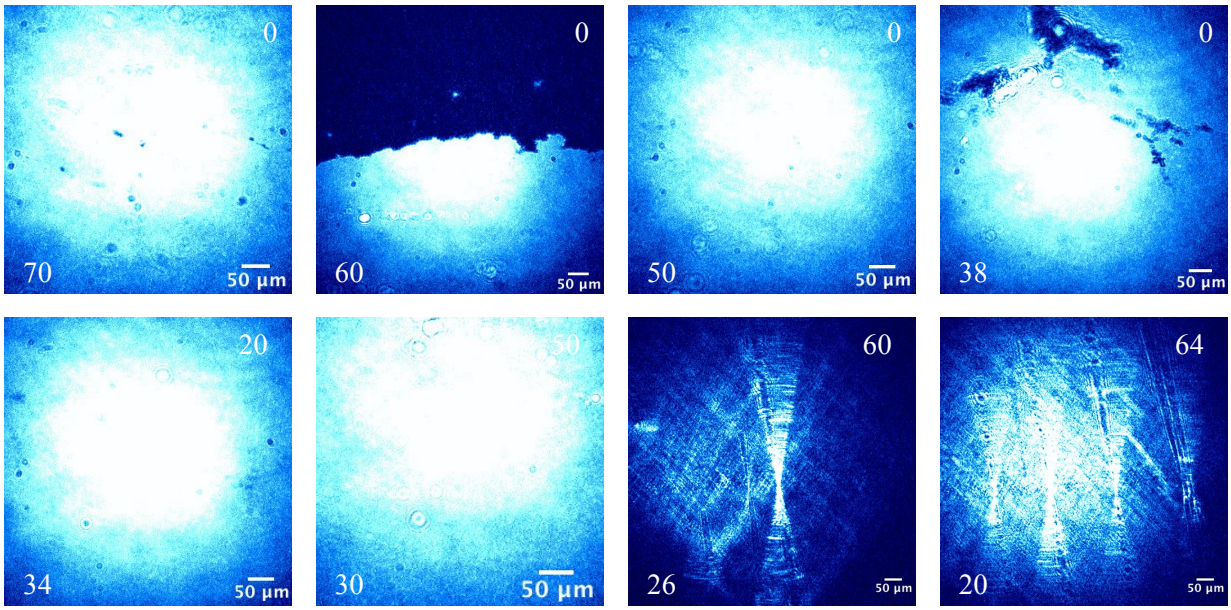


**Figure 4.28.** BAM images of porcine cerebrosides monolayer during compression.

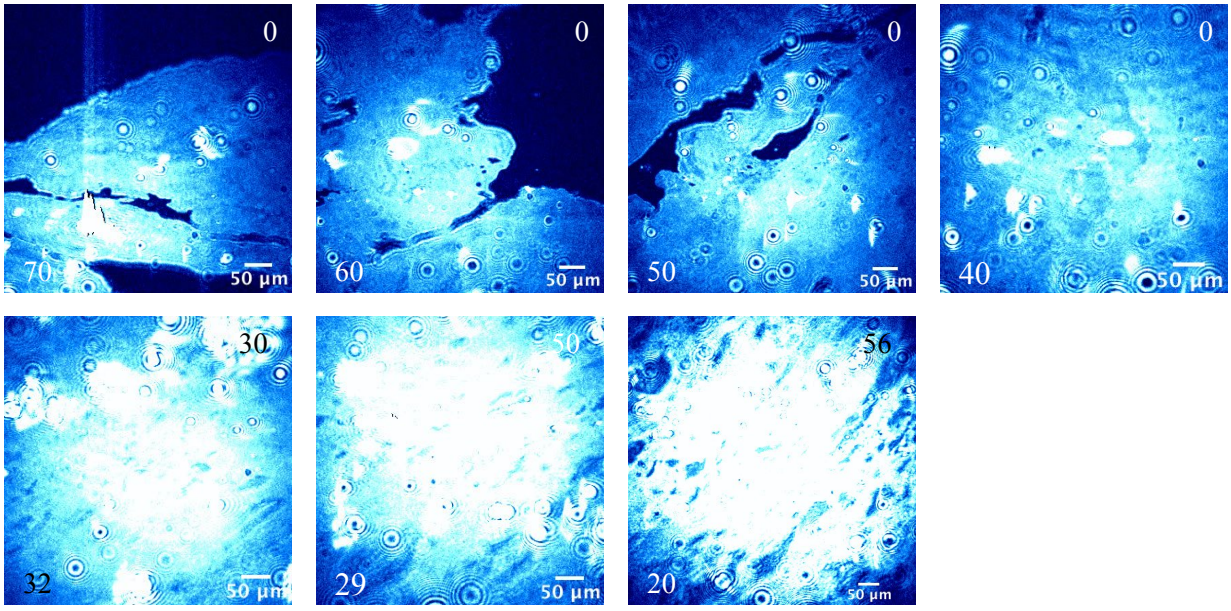


**Figure 4.29.** BAM images of 1:10 cholesterol/bovine cerebrosides mixed monolayer during compression

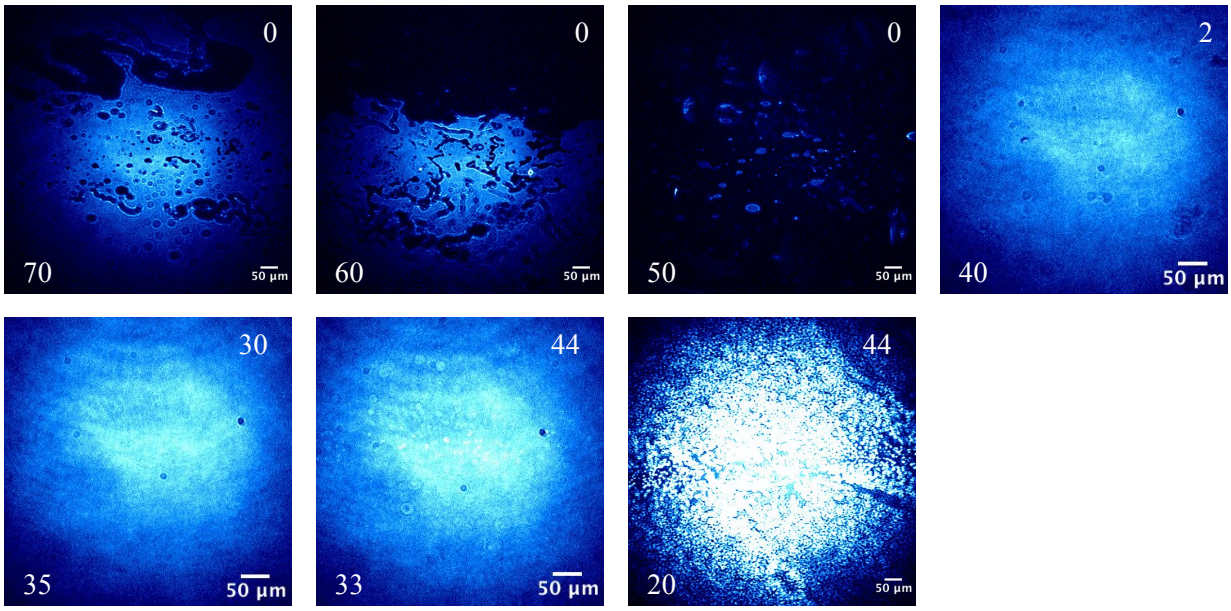


**Figure 4.30.** BAM images of 1:3 cholesterol/bovine cerebrosides mixed monolayer during compression

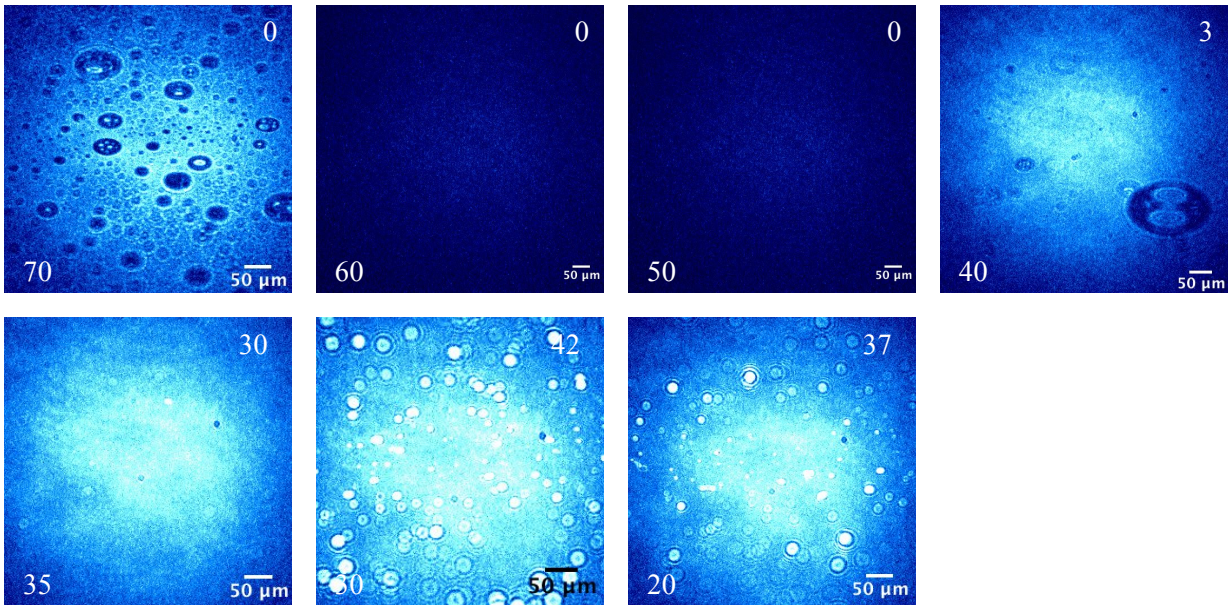


**Figure 4.31.** BAM images of 1:1 cholesterol/bovine cerebrosides mixed monolayer during compression

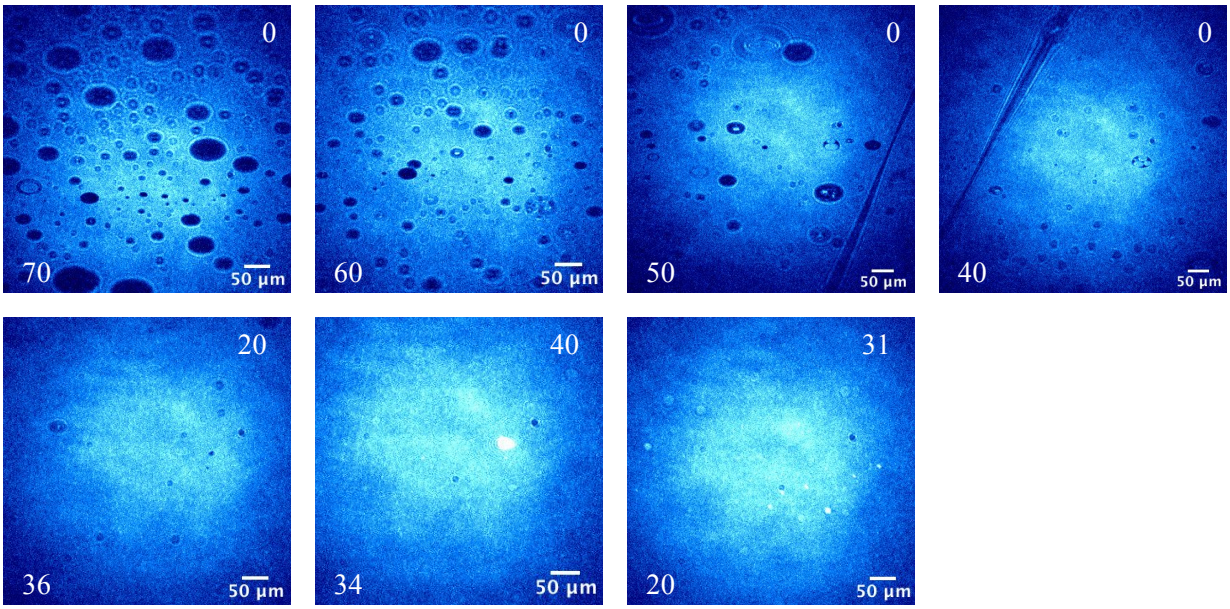


**Figure 4.32.** BAM images of 2:1 cholesterol/bovine cerebrosides mixed monolayer during compression.

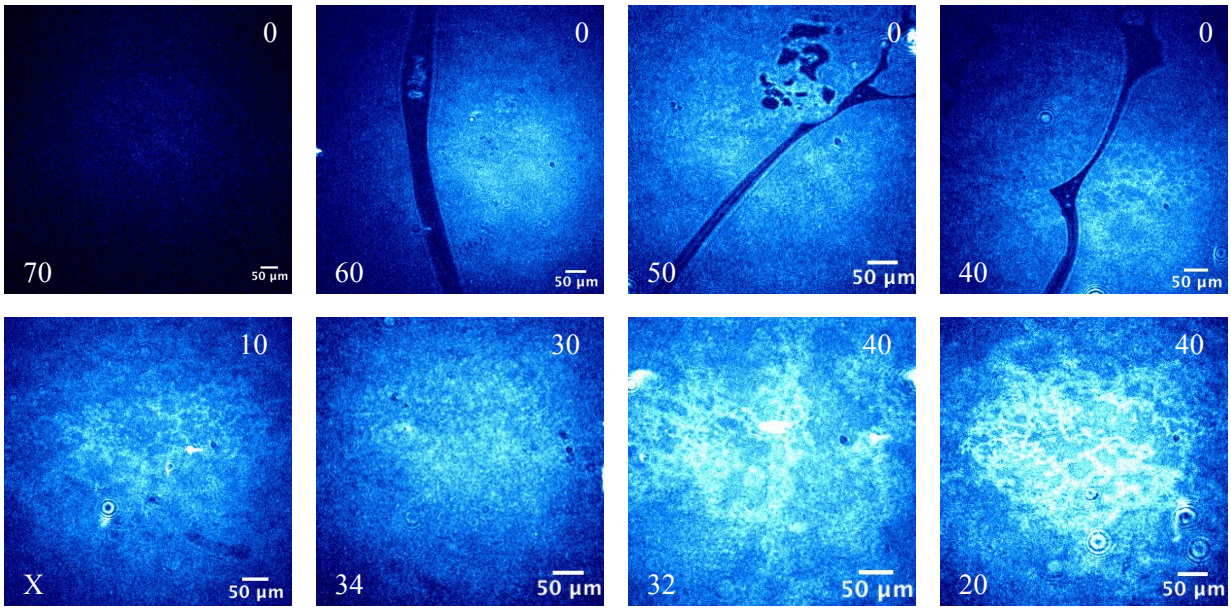


**Figure 4.33.** BAM images of 4:1 cholesterol/bovine cerebrosides mixed monolayer during compression.

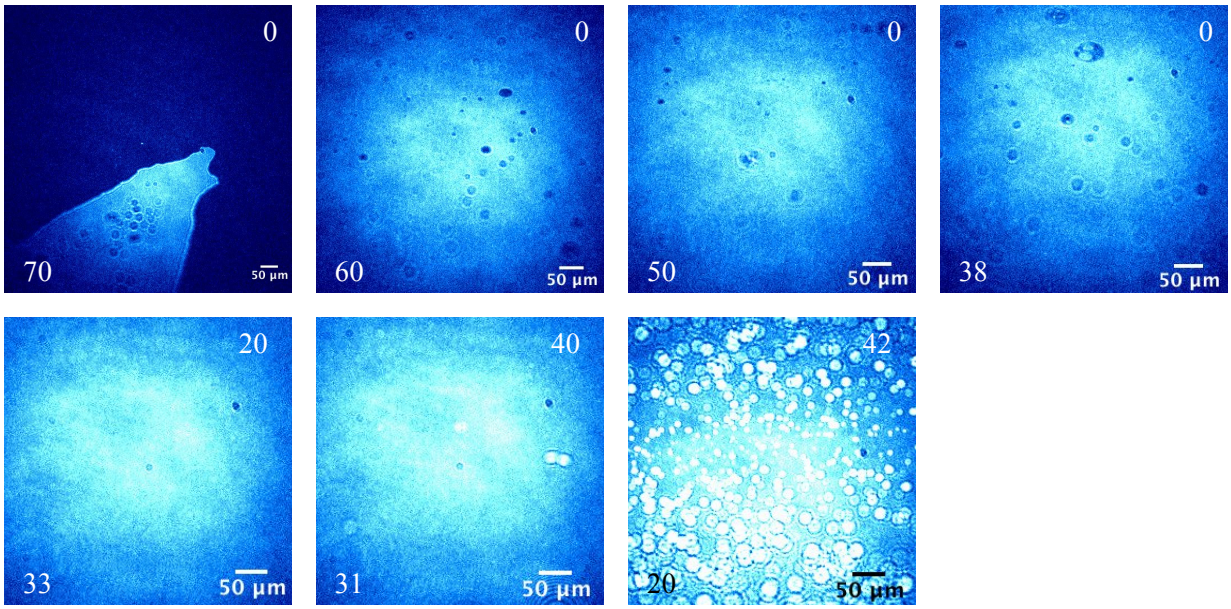


**Figure 4.34.** BAM images of 1:1 cholesterol/porcine cerebrosides mixed monolayer during compression.

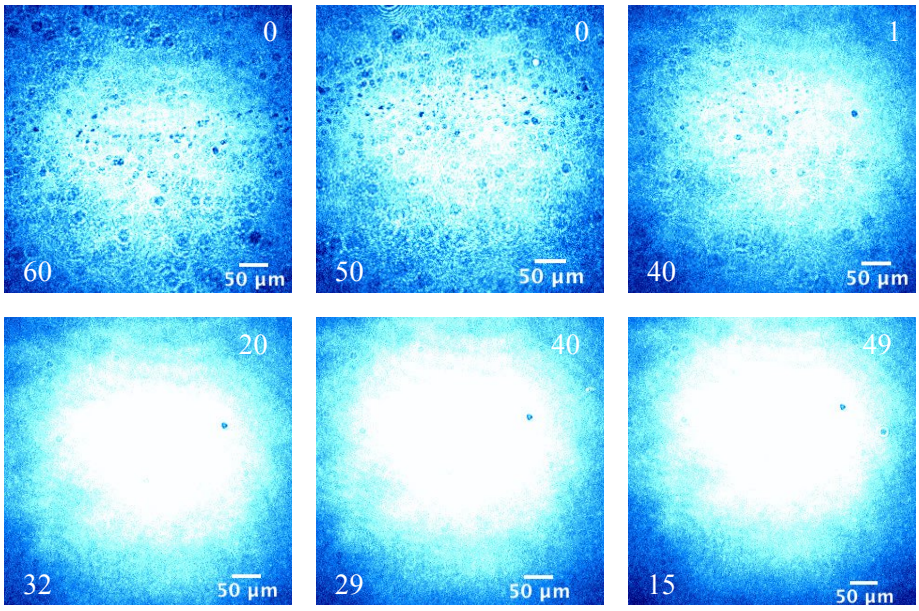


**Figure 4.35.** BAM images of 1:4 palmitic acid/porcine cerebrosides mixed monolayer during compression

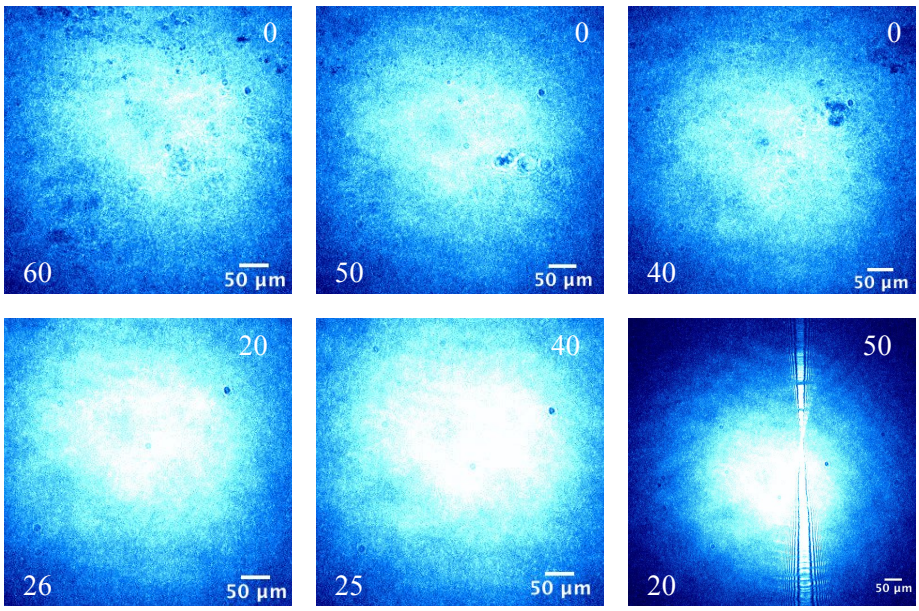


**Figure 4.36.** BAM images of 2:3 palmitic acid/porcine cerebrosides mixed monolayer during compression.

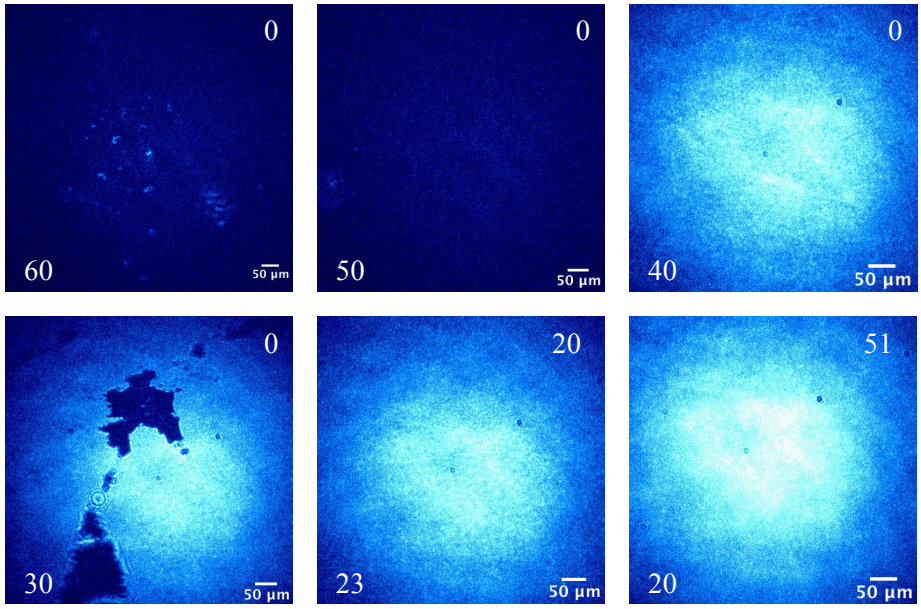


**Figure 4.37.** BAM images of 3:2 palmitic acid/porcine cerebrosides mixed monolayer during compression.

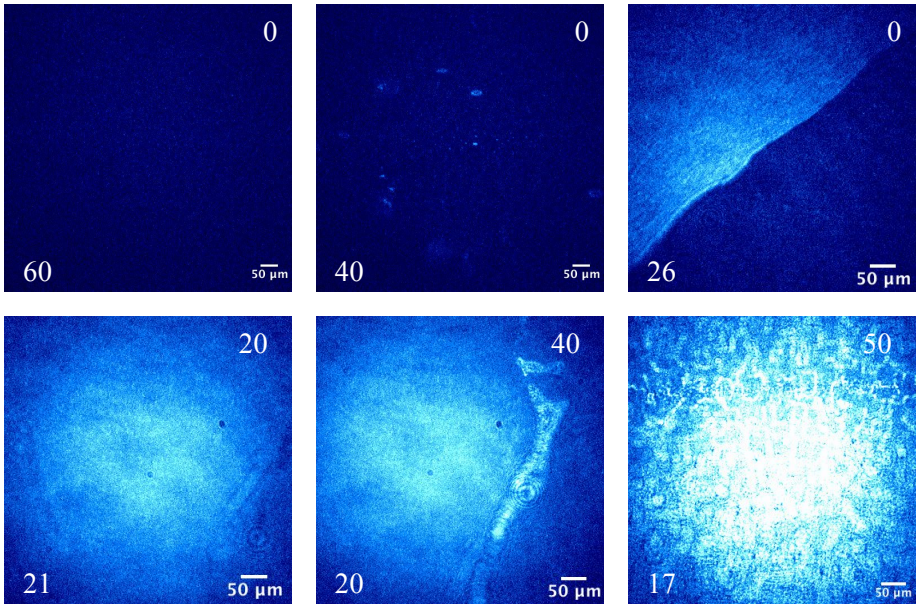


**Figure 4.38.** BAM images of 4:1 palmitic acid/porcine cerebrosides mixed monolayer during compression.

# Chapter 5 Conclusions and Future Work

In this thesis, the surface morphology of bovine and porcine cerebrosides monolayers was investigated. In addition, the effect of chemical composition on the phase behavior, morphology, and miscibility of binary mixtures of cholesterol/Bcerebrosides, and PA/Pcerebrosides were studied by means of surface pressure-area isotherms and BAM. It was found that bovine and porcine cerebrosides have similar surface morphologies. Binary mixtures showed a definitive dependency on the chemical composition, as phase behavior and collapse structures varied with mole fraction cholesterol or PA. All mixtures were determined to be miscible.

Bovine and porcine cerebrosides displayed similar phase behavior and surface morphologies despite differences in chemical composition. Cerebrosides have large, irregular shaped domains at low surface pressures. The collapse structures were both a line shaped structure, but differ slightly in appearance based on composition.

For binary mixtures of cholesterol and Bcerebrosides there was no distinct trend in phase behavior. At a zero surface pressure domain appearance varied with cholesterol content, where an increase in cholesterol content resulted in more cholesterol character in the domains. Collapse pressures and structures varied from those of the cholesterol and Bcerebrosides. Small white aggregates structures were most commonly seen, but other

collapse structures include web-like patterns. Based on the collapse pressures, structures, and thermodynamic analysis mixtures of cholesterol and Bcerebrosides are miscible.

Interactions in the cholesterol/Bcerebrosides films varied depending upon the composition of the film. This suggests that the content of cerebroside and cholesterol in the stratum corneum (SC) will influence intermolecular interactions within the intercellular lipids. The film composition that best represented the human SC lies in the region in which repulsive interactions were observed. Birds on the other hand, whether from a desert or mesic environment, have compositions in which attractive interactions were observed. Such an observation suggests that birds may have better water homestasis within their SC than humans with Gaucher's disease because the lipids interact more favorably at these compositions.

Collapse pressures and surface morphology of PA/Pcerebrosides films indicated that the two components are miscible. Phase behavior of the mixtures was observed to lie between those of the pure components. This condensing effect is most likely facilitated by hydrogen bonding of the headgroups. Surface morphology of mixtures in low pressure regimes varied little from pure Pcerebrosides, also suggesting hydrogen bonding of headgroups occurs. Condensation of these films could have considerable effects on the morphological, optical, and chemical properties in terms of aerosols. Formation of pores within the organic layer could occur, which would facilitate uptake and evaporation of water, and hence influence the size of aerosols. Compared to cholesterol, the Gibbs energy of mixing was substantially less for PA, which suggests that the interaction of

cerebrosides with fatty acids is more favorable than cholesterol. This has implications in the SC, where cholesterol is much more abundant than fatty acids.

Future work for this study includes vibrational spectroscopy of the mixed monolayers. Surface-specific techniques such as infrared reflection absorption spectroscopy (IRRAS) or vibrational sum frequency generation (VSFG) can provide information on the organization and orientation of molecules, especially if isotopes are used.

# References


1. Sadhu, D. P. Correlation between the Lactose Content of Milk and the Cerebroside and Choline Content of Brain. *J. Dairy Sci.* **31,** 347–351 (1948).
2. Cateni, F., Zilic, J., Falsone, G., Scialino, G. & Banfi, E. New Cerebrosides from Euphorbia peplis L.: Antimicrobial Activity Evaluation. *Bioorganic & Medicinal Chemistry Letters* **13,** 4345–4350 (2003).
3. Nakahara, H. *et al.* Cerebroside Langmuir monolayers originated fromt echinoderms I. Binary systems of cerebrosides and phospholipids. *Colloid Surface B* **42,** 157–174 (2005).
4. Munoz-Garcia, A., Ro, J., Brown, J. C. & Williams, J. B. Identification of complex mixtures of sphingolipids in the stratum corneum by reversed-phase high-performance liquid chromatography and atmospheric pressure photospray ionization mass spectrometry. *J. Chromatogr. A.* **1133,** 58–68 (2006).
5. Tiemeyer, M., Yasuda, Y. & Schnaars, R. L. Ganglioside-specific Binding Protein on Rat Brain Membranes. *J. Biol. Chem.* **264,** 1671–1681 (1989).
6. Kojima, N. & Hakomori, S. Specific Interaction between Gangliotriaosylceramide (Gg3) and Sialosyllactosylceramide (GM3) as a Basis for Specific Cellular Recognition between Lymphoma and Melonoma Cells. *J. Biol. Chem.* **264,** 20159–20162 (1989).
7. Tagami, S. *et al.* Ganglioside GM3 Participates in the Pathological Conditions of Insulin Resistance. *J. Biol. Chem.* **277,** 3085–3092 (2002).
8. Maggio, B. & Cumar, F. A. Experimental allergic encephalomyelitis dissociation of neurological symptoms from lipid alterations in brain. *Nature* **253,** 1975
9. Maggio, B. The Surface Behavior of Glycosphingolipids in Biomembranes: A New Frontier of Molecular Ecology. *Prog Biophys. molec. Biol.* **62,** 55–117 (1994).
10. Yu, R. K., Bieberich, E., Xia, T. & Zeng, G. Regulation of ganglioside biosynthesis in the nervous system. *J. Lipid Res.* **45,** 783–794 (2004).
11. Holleran, W. M. *et al.* Processing of Epidermal Glucosylceramides Is Required for Optimal Mammalian Cutaneous Permeability Barrier Function. *J. Clin. Invest.* **91,** 1656–1664 (1993).
12. Champagne, A. *et al.* Lipid composition of the stratum corneum and cutaneous water loss in bird along an aridity gradient. *J. Exp. Biol.* **215,** 4299–4307 (2012).
13. Michaelson, L. V., Dunn, T. M. & Napier, J. A. Viral trans-dominant manipulation of algal sphingolipids. *Trends Plant Sci.* **15,** 651–655 (2010).

14. Facchini, M. C. *et al.* Primary Submicron Marine Aerosol Dominated by Insoluble Organic Colloids and Aggregates. *Geophys. Res. Lett.* **35,** L17814 (2008).
15. Lawrence, J. R., Glass, S. V. & Nathanson, G. M. Evaporation of Water through Butanol Films at the Surface of Supercooled Sulfuric Acid. *J. Phys. Chem. A* **109,** 7449–7457 (2005).
16. Beaver, M. R., Freedman, M. A., Hasenkopf, C. A. & Tolbert, M. A. Cooling Enhancement of Aerosol Particles Due to Surfactant Precipitation. *J. Phys. Chem. A* **114,** 7070–7076 (2010).
17. Tervahattu, H., Juhanoja, J. & Kupiainen, K. Identification of an organic coating on marine aerosol particles by TOF-SIMS. *J. Geophys. Res.* **107,** (2002).
18. Verbalis, J. G. Disorders of body water homeostasis. *Best Prac. Res. Cl. En.* **17,** 471–503 (2003).
19. Goldsmith, Paller, A. S., Katz, S. I., Leffell, D. J. & Wolff, K. *Fitzpatrick's Dermatology in General Medicine*. (The McGraw-Hill Companies, Inc, 2012).
20. Gartner, L. P. & Hiatt, J. L. *Color Textbook of Histology*. (W.B. Saunders Company, 2001).
21. Williams, J. B., Munoz-Garcia, A. & Champagne, A. Climate change and cutaneous water loss in birds. *J. Exp. Biol.* **215,** 1053–1060 (2012).
22. Winsor, T. & Burch, G. E. Differential Roles of Layers Of Human Epigastric Skin On Diffusion Rate of Water. *Arch. Intern. Med.* **74,** 428–436 (1944).
23. Michaels, A. S., Chandrasekaran, S. K. & Shaw, J. E. Drug Permeation Through Human Skin: Theory and in Vitro Experimental Measurement. *AIChe Journal* **21,** 985–996 (1975).
24. Elias, P. M., Cooper, E. R., Korc, A. & Brown, B. E. Percutaneous Transport in Relation to Stratum Corneum Structure and Lipid Composition. *J. Invest. Dermatol.* **76,** 297–301 (1981).
25. Wickett, R. R. & Visscher, M. O. Structure and Fuction of the Epidermal Barrier. *Am. J. Infect. Control* **34,** S98–S110 (2006).
26. Proksch, E., Brandner, J. M. & Jensen, J. The skin; an indispensable barrier. *Exp. Dermatol.* **17,** 1063–1072 (2008).
27. Forslind, B. A Domain Mosaic Model of the Skin Barrier. *Acta Derm Venereol* **74,** 1–6 (1994).
28. Wertz, P. W. Lipids and barrier function of the skin. *Acta Derm Venereol* **208,** 7–11 (2000).
29. Bouwstra, J. A., Dubbelaar, F. E. R., Gooris, G. S. & Ponec, M. The Lipid Organisation in the Skin Barrier. *Acta Derm Venereol* **208,** 23–30 (2000).
30. Norlen, L. Skin Barrier Structure and Function: The Single Gel Phase Model. *J. Invest. Dermatol.* **117,** 830–836 (2001).
31. Onken, H. D. & Moyer, C. A. The Water Barrier in Human Epidermis. *Arch. Dermatol.* **87,** (1963).
32. Matoltsy, A. G., Downes, A. M. & Sweeney, T. M. Studies of the Epidermal Water Barrier. Part II. Investigation of the Chemical Nature of the Water Barrier. *J. Invest. Dermatol.* **50,** 19–26 (1968).

33. Sweeney, T. M. & Downing, D. T. The Role of Lipids in the Epidermal Barrier to Water Diffusion. *J. Invest. Dermatol.* **55,** 135–140 (1970).
34. *Bioengineering of the Skin: Water and the Stratum Corneum*. (CRC Press, 1994).
35. Gray, G. M. & Yardley, H. J. Lipid Composition of Cells Isolated from Pig, Human, and Rat Epidermis. *J. Lipid Res.* **16,** 434–440 (1975).
36. Wertz, P. W. The nature of the epidermal barrier: biochemical aspects. *Adv. Drug Deliver. Rev.* **18,** 283–294 (1996).
37. Grayson, S. *et al.* Lamellar Body-Enriched Fractions from Neonatal Mice: Preparative Techniques and Partial Characterization. *J. Invest. Dermatol.* **85,** 289–294 (1985).
38. Freinkel, R. K. & Traczyk, T. N. Lipid Composition and Acid Hydrolase Content of Lamellar Granules of Fetal Rat Epidermis. *J. Invest. Dermatol.* **85,** 295–298 (1985).
39. Yardley, H. J. & Summerly, R. Lipid Composition and Metabolism in Normal and Diseased Skin. *Pharmac. Ther.* **13,** 357–383 (1981).
40. Madison, K. C. Barrier Function of the Skin: 'La Raison d'Etre' of the Epidermis. *J. Invest. Dermatol.* **121,** 231–241 (2003).
41. Lampe, M. A. *et al.* Human stratum corneum lipids: characterisation and regional variations. *J. Lipid Res.* **24,** 120–130 (1983).
42. Wertz, P. W., Swartzendruber, D. C., Madison, K. C. & Downing, D. T. Composition and Morphology of Epidermial Cyst Lipids. *J. Invest. Dermatol.* **89,** 419–425 (1987).
43. Norlen, L., Nicander, I. & Lundsjoe, A. A new HPLC-based method for the quantitative analysis of inner stratum corneum lipids with special reference to the free fatty acid fraction. *Arch Dermatol Res* **290,** 508–516 (1998).
44. Wertz, P. W. & Van den Bergh, B. The physical, chemical, and functional properties of lipids in the skin and other biological barriers. *Chem. Phys. Lipids* **91,** 85–96 (1998).
45. *Cholesterol in Membrane Models*. (CRC Press, 1993).
46. Wertz, P. W., Miethke, M. C., Long, S. A., Strauss, J. S. & Downing, D. T. The Composition of the Ceramides from Human Stratum Corneum and from Comedones. *J. Invest. Dermatol.* **84,** 410–412 (1985).
47. Flach, C. R., Mendelsohn, R., Rerek, M. E. & Moore, D. J. Biophysical Studies of Model Stratum Corneum Lipid Monolayers by Infrared Reflection-Absorption Spectroscopy and Brewster Angle Microscopy. *J. Phys. Chem. B* **104,** 2159–2165 (2000).
48. Goni, F. M. & Alonso, A. Biophysics of sphingolipids I. Membrane properties of sphingosine, ceramides, and other simple sphingolipids. *Biochim. Biophys. Acta* **1758,** 1902–1921 (2006).
49. Munoz-Garcia, A. & Williams, J. B. Cutaneous water loss and lipids of the stratum corneum in house sparrows Passer domesticus from arid and mesic environments. *J. Exp. Biol.* **208,** 3689–3700 (2005).
50. Ro, J. & Williams, J. B. Respiratory and cutaneous water loss of temperate-zone passerine birds. *Comp. Biochem. Physiol. A* **156,** 237–246 (2010).

51. Kipps, T. J., Lichtman, M. A., Seligsohn, U., Kaushansky, K. & Prchal, J. T. *Williams Hematology*. (The McGraw-Hill Companies, Inc, 2010).
52. Fuster, V., Walsh, R. A. & Harrington, R. A. *Hurst's The Heart*. (The McGraw-Hill Companies, Inc, 2011).
53. Brunicardi, F. C. *et al. Schwart'z Principles of Sugery*. (The McGraw-Hill Companies, Inc, 2010).
54. Holleran, W. M. *et al.* Consequences of Beta-Glucocerebrosidase Deficiency in Epidermis. *J. Clin. Invest.* **93,** 1756–1764 (1994).
55. Biegstraaten, M. *et al.* The cognitive profile of type 1 Gaucher disease patients. *J Inherit Metab Dis* **35,** 1093–1099 (2012).
56. Lui, K., Commens, C., Choong, R. & Jaworski, R. Collodion babies with Gaucher's disease. *Arch. Dis. Child.* **63,** 854–856 (1988).
57. Lipson, A. H., Rogers, M. & Berry, A. Collodion babies with Gaucher's disease-a further case. *Arch. Dis. Child.* **66,** 667 (1991).
58. Fujimoto, A., Tayebi, N. & Sidransky, E. Congenital Ichthyosis Preceding Neurologic Symptoms in Two Sibs With Type 2 Gaucher Disease. *Am. J. Med. Genet.* **59,** 356–358 (1995).
59. Stone, D. L. *et al.* Type 2 Gaucher disease: the collodion baby phenotype revisited. *Arch Dis Child Fetal Neonatal Ed* **82,** F163–F166 (2000).
60. Tybulewicz, V. L. J. *et al.* Animal model of Gaucher's disease from targeted disruption of the mouse glucocerebrosidase gene. *Nature* **357,** 407–410 (1992).
61. Sidransky, E. *et al.* Epidermal Abnormalities May Distinguish Type 2 from Type 1 and Type 2 Gaucher Disease. *Pedriatr. Res.* **39,** 134–141 (1996).
62. Elias, P. M., Brown, B. E. & Ziboh, V. A. The Permeability Barrier in Essential Fatty Acid Deficiency: Evidence for a Direct Role for Linoleic Acid in Barrier Function. *J. Invest. Dermatol.* **74,** 230–233 (1980).
63. Hardy, J. T. The Sea Surface Microlayer: Biology, Chemistry, and Anthropogenic Enrichment. *Prog. Oceanogr.* **11,** 307–328 (1982).
64. Gade, M., Alpers, W., Masuko, H. & Kobayashi, T. Imaging of biogenic and anthropogenic ocean surface films by the multifrequency/mulitpolarization SIR-C/X-SAR. *J. Geophys. Res.* **103,** 18851–18866 (1998).
65. Matsumoto, K. & Uematsu, M. Free Amino Acids in Marine Aerosols over the Western North Pacific. *Atmos. Envrion.* **39,** 2163–2170 (2005).
66. Donaldson, D. J. & Vaida, V. The Influence of Organic Films at the Air-Aqueous Boundary on Atmospheric Processes. *Chem. Rev.* **106,** 1445–1461 (2006).
67. Li, W. K. W. Annual average abundance of heterotrophic bacteria and Synechococcus in surface ocean waters. *Limnol. Oceanogr.* **43,** 1746–1753 (1998).
68. Weinbauer, M. G. & Rassoulzadegan, F. Are viruses driving microbial diversification and diversity. *Environ. Microbiol.* **6,** 1–11 (2004).
69. Hawkins, L. N. & Russell, L. M. Polysaccharides, Proteins, and Phytoplankton Fragments: Four Chemically Distinct Types of Marine Primary Organic Aerosol Classified by Single Particle Spectromicroscopy. *Advances in Meterology* (2010).
70. Tervahattu, H. *et al.* New evidence of an organic layer on marine aerosols. *J. Geophys. Res.* **107,** AAC 1–1 (2002).

71. Ellison, G. B., Tuck, A. F. & Vaida, V. Atmospheric processing of organic aerosols. *J. Geophys. Res.* **104,** 11633–11641 (1999).
72. Dobson, C. M., Ellison, G. B., Tuck, A. F. & Vaida, V. Atmospheric aerosols as prebiotic chemical reactors. *PNAS* **97,** 11864–11868 (2000).
73. Kovac, N., Bajit, O., Faganeli, J., Sket, B. & Orel, B. Study of macroaggregate composition using FT-IR and 1H-NMR spectroscopy. *Mar. Chem.* **78,** 205–215 (2002).
74. Ziemann, P. J. Phase matters for aerosols. *Nature* **467,** 797–798 (2010).
75. Garland, R. M. *et al.* Impact of palmitic acid coating on the water uptake and loss of ammonium sulfate particles. *Atmos. Chem. Phys.* **5,** 1951–1961 (2005).
76. Muralidhar, P., Radhika, P., Krishna, N., Rao, D. V. & Rao, C. B. Sphingolipids from Marine Organisms: A Review. *Natural Product Sciences* **9,** 117–142 (2003).
77. Pagarete, A., Allen, M. J., Wilson, W. H., Kimmance, S. A. & De Vargas, C. Host-virus shift of the sphingolipid pathway along an Emiliania huxleyi bloom: survival of the fattest. *Environ. Microbiol.* **11,** 2840–2848 (2009).
78. Vardi, A. *et al.* Host-virus dyanmics and subcellular controls of cell fate in a natural coccolithophore population. *PNAS* **109,** 19327–19332 (2012).
79. Chattoraj, D. K. & Birdi, K. S. *Adsorption and The Gibbs Surface Excess*. (Plenum Press, 1984).
80. Gaines, G. L., Jr. *Insoluble Monolayers at Liquid-Gas Interfaces*. (Interscience Publishers, 1966).
81. Hu, Y. F., Lee, K. Y. C. & Israelachvili, J. Sealed minitrough for microscopy and long-term stability studies of Langmuir monolayers. *Langmuir* **19,** 100–104 (2003).
82. Kwok, D. Y., Vollhardt, D., Miller, R., Li, D. & Neumann, A. W. Axisymmetric drop shape analysis as a film balance. *Colloid Surface A* **88,** 51–58 (1994).
83. Stauffer, C. E. The Measurement of Surface Tension by the Pendant Drop Technique. *J. Phys. Chem.* **69,** 1933–1938 (1965).
84. Hansen, F. K. & Rodsrud, G. Surface Tension by Pendant Drop. *J. Colloid Interf. Sci.* **141,** 1–9 (1991).
85. Saad, S. M. I., Policova, Z. & Neumann, A. W. Design and accuracy of pendant drop method for surface tension measurements. *Colloid Surface A* **284,** 442–452 (2011).
86. Del Rio, O. I. & Neumann, A. W. Axisymmetric Drop Shape Analysis: Computational Methods for the Measurement of Interfacial Properties from the Shape and Dimensions of Pendant and Sessile Drops. *J. Colloid Interf. Sci.* **196,** 136–147 (1997).
87. Yu, L. M. Y. *et al.* Constrained sessile drop as a new configuration to measure low surface tension in lung surfactant systems. *J. Appl. Physiol.* **97,** 704–715 (2004).
88. Saad, S. M. I. *et al.* A double injection ADSA-CSD methodology for lung surfactant inhibition and reversal studies. *Colloid Surface B* **73,** 365–375 (2009).
89. Kang, N. *et al.* Interaction between chitosan and bovine lung extract surfactants. *Biochim. Biophys. Acta* **1778,** 291–302 (2008).
90. Smith, R. & Berg, J. C. The Collapse of Surfactant Monolayers at the Air-Water Interface. *J. Colloid Interf. Sci.* **74,** 273–286 (1980).

91. Gopal, A. & Lee, K. Y. C. Morphology and Collapse Transitions in Binary Phospholipid Monolayers. *J. Phys. Chem. B* **105,** 10348–10354 (2001).
92. Ybert, C., Lu, W., Moeller, G. & Knobler, C. M. Collapse of a Monolayer by Three Mechanisms. *J. Phys. Chem. B* **106,** 2004–2008 (2002).
93. Ma, G. & Allen, H. C. Condensing Effect of Palmitic Acid on DPPC in Mixed Langmuir Monolayers. *Langmuir* **23,** 589–597 (2007).
94. Lipp, M. M., Lee, K. Y. C., Takamoto, D. Y., Zasadzinski, J. A. & Waring, A. J. Coexistence of Buckled and Flat Monolayers. *Phys. Rev. Lett.* **81,** 1650–1653 (1998).
95. Lee, K. Y. C. Collapse Mechanisms of Langmuir Monolayers. *Annu. Rev. Phys. Chem.* **59,** 771–791 (2008).
96. Tchoreloff, P., Gulik, A., Denizot, B., Proust, J. E. & Puisieux, F. A structural study of interfacial phospholipid and lung surfactant layers by tranmission electron microscopy after Blodgett sampling: influence of surface pressure and temperature. *Chem. Phys. Lipids* **59,** 151–165 (1991).
97. Lipp, M. M., Lee, K. Y. C., Waring, A. & Zasadzinski, J. A. Fluorescence, Polarized Fluoresence, and Brewster Angle Microscopy of Palmitic Acid and Lung Surfactant Protein B Monolayers. *Biophys. J.* **72,** 2783–2804 (1997).
98. Nguyen, T. T., Gopal, A., Lee, K. Y. C. & Witten, T. A. Surface charge relaxation and the pearling instability of charged surfactant tubes. *Physical Review E* **72,** 051930 (2005).
99. Vaknin, D., Bu, W., Satija, S. K. & Travesset, A. Ordering by Collapse: Formation of Bilayer and Trilayer Crystals by Folding Langmuir Monolayers. *Langmuir* **23,** 1888–1897 (2007).
100. Lu, W., Knobler, C. M. & Bruinsma, R. F. Folding Langmuir Monolayers. *Phys. Rev. Lett.* **89,** 146107 (2002).
101. Baoukina, S., Motincelli, L., Risselada, H. J., Marrink, S. J. & Tieleman, D. P. The molecular mechanism of lipid monolayer collapse. *PNAS* **105,** 10803–10808 (2008).
102. Chou, T. & Chang, C. Thermodynamic behavior and relaxation processes of mixed DPPC/cholesterol monolayers at the air/water interface. *Colloid Surface B* **17,** 71–79 (2000).
103. Ding, J. Q., Takamoto, D. Y., Von Nahmen, A., Lipp, M. M. & Lee, K. Y. C. Effects of lung surfactant proteins, SP-B and SP-C, and palmitic acid on monolayer stability. *Biophysical Journal* **80,** 2262–2272 (2001).
104. Marshall, G., Dennin, M. & Knobler, C. M. A compact Brewster-angle microscope for use in Langmuir-Blodgett deposition. *Review of Scientific Instruments* **69,** 3699 (1998).
105. Lheveder, C., Henon, S., Mercier, R., Tissot, G. & Fournet, P. A new Brewster angle microscope. *Review of Scientific Instruments* **69,** 1446 (1998).
106. Fowles, G. R. *Introduction to Modern Optics*. (Dover Publicatons, Inc., 1975).
107. Ingle, Jr., J. D. & Crouch, S. R. *Spectrochemical Analysis*. (Prentice Hall, 1988).
108. Hecht, E. *Optics*. (Addison Wesley, 2002).

109. Henon, S. & Meunier, J. Microscope at the Brewster angle: Direct observation of first order phase transitions in monolayers. *Review of Scientific Instruments* **62,** 936 (1991).
110. Johnston, D. S., Coppard, E. & Chapman, D. A Langmuir film balance study of the interactions of ionic and polar solutes with glycolipid monolayers. *Biochim. Biophys. Acta* **815,** 325–333 (1985).
111. Adam, N. K., Aksew, F. A. & Danielli, J. F. CCX. Further Experiments on Surface Films of Sterols and Their Derivatives. *Biochem. J.* (1935).
112. Cadena-Nava, R. D., Martin-Mirones, J. M., Vazquez-Martinez, E. A., Roca, J. A. & Ruiz-Garcia, J. Direct Observations of phase changes in Langmuir films of Cholesterol. *Rev. Mex. Fis.* **52,** 32–40 (2006).
113. Nutting, G. C. & Harkins, W. D. Pressure-Area Relations of Fatty Acid and Alcohol Monolayers. *J. Am. Chem. Soc.* **61,** 1180–1187 (1939).
114. Johnston, D. S. & Chapman, D. The Properties of Brain Galactocerebroside Monolayers. *Biochim. Biophys. Acta* **937,** 10–22 (1988).
115. Slotte, J. P., Ostman, A., Kumar, E. R. & Bittmann, R. Cholesterol Interacts with Lactosyl and Maltosyl Cerebrosides but Not with Glucosyl or Galactosyl Cerebrosides in Mixed Monolayers. *Biochemistry* **32,** 7886–7892 (1993).
116. Korchowiec, B., Korchowiec, J., Hato, M. & Rogalska, E. Glycolipid-Cholesterol monolayers: Towards a better understanding of the interaction between the membrane components. *Biochim. Biophys. Acta* **1808,** 2466–2476 (2011).
117. Motomura, K., Teranzono, T., Matuo, H. & Matuura, R. Mixed Monolayers of Cholesterol with Fatty Acids. *J. Colloid Interf. Sci.* **57,** 52–57 (1976).
118. Baglioni, P., Cestelli, G., Dei, L. & Gabrielli, G. Monolayers of Cholesterol at Water-Air Interface: Mechanims of Collapse. *J. Colloid Interf. Sci.* **104,** 143–150 (1985).
119. Seoane, R. *et al.* Thermodynamic and Brewster Anlge Microscopy Stuides of Fatty Acid/Cholesterol Mixtures at the Air-Water Interface. *J. Phys. Chem. B* **104,** 7735–7744 (2000).
120. Ohe, C., Sasaki, T., Noi, M., Goto, Y. & Itoh, K. Sum Frequency Generation Spectrscopic Study of the Condensation Effect of Cholesterol on a Lipid Monolayer. *Anal Bioanal Chem* **388,** 2007
121. Tang, C. & Allen, H. C. Ionic Binding of Na+ versus K+ to the Carboxylic Acid Headgroup of Palmitic Acid Monolayers Studied by Vibrational Sum Frequency Generation Spectroscopy. *J. Phys. Chem. A* **113,** 7383–7393 (2009).
122. Sierra-Hernandez, M. R. & Allen, H. C. Incorporation and Exclusion of Long Chain Alkyl Halides in Fatty Acid Monolayers at the Air-Water Interface. *Langmuir* **26,** 18806–18816 (2010).
123. Kaganer, V. M., Moehwald, H. & Dutta, P. Structure and Phase Transitions in Langmuir Monolayers. *Reviews of Modern Physics* **71,** 779–819 (1999).
124. Nakahara, H. *et al.* Cerebroside Langmuir monolayers originated from the echinoderms: II. Binary systems of cerebrosides and steroids. *Colloids and Surfaces B: Biointerfaces* **42,** 175–185 (2005).

125. Qi, S., Roser, S. J., Deutsch, D., Barker, S. A. & Craig, D. Q. M. A Laser Imaging and Neutron Reflection Investigation Into the Monolayer Behavior of Fatty Acids Used for Taste Making Microspheres. *Journal of Pharmaceutical Sciences* **97,** 1864–1877 (2008).
126. Rosetti, C. M., Oliveira, R. G. & Maggio, B. Reflectance and Topography of Glycosphingolipid Monolayers at the Air-Water Interface. *Langmuir* **19,** 377–384 (2003).
127. Ries, Jr., H. E. Heart-Shaped Monolayer Islands and Ridged Collapse Structures of Ceramide Galactose. *J. Colloid Interf. Sci.* **88,** 298–301 (1982).